

Banner appropriate to article type will appear here in typeset article

Mixing as a correlated aggregation process

J. Heyman, E. Villermaux, P. Davy & T. Le Borgne

(Received xx; revised xx; accepted xx)

Mixing describes the process by which solutes evolve from an initial heterogeneous state to uniformity under the stirring action of a fluid flow. Fluid stretching forms thin scalar lamellae which coalesce due to molecular diffusion. Owing to the linearity of the advection-diffusion equation, coalescence can be envisioned as an aggregation process. Here, we demonstrate that in smooth two-dimensional chaotic flows, mixing obeys a correlated aggregation process, where the spatial distribution of the number of lamellae in aggregates is highly correlated with their elongation and is set by the fractal properties of the advected material lines. We show that the presence of correlations makes mixing less efficient than a completely random aggregation process because lamellae with similar elongations and scalar levels tend to remain isolated from each other. We show that correlated aggregation is uniquely determined by a single exponent which quantifies the effective number of random aggregation events. These findings expand aggregation theories to a larger class of systems, which have relevance to various fundamental and applied mixing problems.

1. Introduction

Mixing of solutes by the stirring action of a fluid flow is ubiquitous to many natural and industrial processes (Ottino 1990). The evolution of the solute concentration c in an incompressible velocity field \mathbf{v} is governed by the conservation equation

$$\partial_t c + \mathbf{v} \cdot \nabla c = \kappa \nabla^2 c, \quad (1.1)$$

with κ the molecular diffusivity. While advected by the flow, the solute also *mixes* with its surrounding due to the irreversible effect of molecular diffusion, and concentration tends to homogenize.

Although fully linear, Eq. 1.1 is characterized by rich spatio-temporal behaviors, that have retained considerable attention along the years (Warhaft 2000; Falkovich *et al.* 2001; Rothstein *et al.* 1999). As illustrated in Fig. 1a, an initial blob of passive solute repeatedly stirred in a chaotic flow produces scalar filaments that stretch exponentially in time (Aref 1984). Their thickness is blocked at the so-called Batchelor scale, scale at which molecular diffusion compensates the effect of stretching on scalar gradients (Batchelor 1959). Owing to flow incompressibility, these filaments are also exponentially compressed onto each other, leading to their diffusive coalescence (Fig. 1b). These three processes –stretching, diffusion and coalescence– are key to quantify and predict the statistics of c in the homogenizing mixture.

Filament stretching and diffusion can be effectively quantified in a Lagrangian frame aligned with the local directions of elongation and compression of the flow field (Ranz 1979; Balkovsky & Fouxon 1999). Such approach, referred to as Lagrangian stretching or lamellar

Abstract must not spill onto p.2

theory, provides a theoretical link between the stretching statistics of the flow (its advective properties) and the evolution of concentration in isolated lamellae. It yields good estimates of the decay of the scalar concentration variance (Haynes & Vanneste 2005; Tsang *et al.* 2005) and of the shape of the scalar pdf in a range of chaotic flows (Meunier & Villermaux 2010). However, it is *a-priori* limited to the early stage of mixing, when scalar filaments evolve far from each-other, that is well before coalescence (Fereday *et al.* 2002; Villermaux & Duplat 2003).

Interestingly, the Lagrangian stretching framework has been shown (Haynes & Vanneste 2005; Tsang *et al.* 2005) to provide correct mixing rate predictions even at asymptotic time, for smooth flow in the so-called Batchelor regime, that is when scalar gradients persist only at small scales. Indeed, in periodic domains, asymptotic mixing rates have been shown to be either controlled "locally" by the stretching of material lines, or "globally" by macro-dispersive flow properties, depending on the domain size with respect to the velocity correlation length. In the "local" case, it is still unknown why the Lagrangian stretching framework would remain accurate after coalescence time, when stretched filaments are not isolated from each other. In addition, it is unknown how stretching statistics controls the shape of the asymptotic scalar pdf. Some theoretical results exist on the limiting shape of scalar pdf (Sinai & Yakhot 1989), but owing to closures that are not trivial to relate to physical properties of the flow (Sukhatme 2004). In turn, Pierrehumbert (1994) and followers Rothstein *et al.* (1999); Sukhatme & Pierrehumbert (2002) have documented the self-similarity of asymptotic scalar pdf through the emergence of a "strange eigenmode", but a physically based modeling of the shape of the scalar pdf is still an open question.

Recognizing the additive nature of scalar coalescence in bounded domains, Villermaux & Duplat (2003) have proposed to describe the late time evolution of concentration pdf by a random aggregation mechanism, whereby the concentration field results from a sum of independent filaments that individually obey Lagrangian stretching dynamics, and that overlap by diffusion. This random aggregation scenario accurately captures the shape of asymptotic scalar pdf (Meunier & Villermaux 2010; Duplat & Villermaux 2008), if one uses the rate of filament aggregation as a fitting parameter. However, no independent measure of filament aggregation in chaotic flows has been obtained so far to validate the random aggregation hypothesis. In addition, it is still unclear if aggregation processes tends to accelerate or decelerate mixing compared to stretching.

Recently, Heyman *et al.* (2021) have proposed that scalar aggregation could obey a correlated process, where poorly stretched regions of the flow containing weakly mixed solutes remain weakly aggregated in proportion. Such intimate correlation between stretching and aggregation has the advantage to explain the persistent role of Lagrangian stretching statistics on asymptotic scalar mixing which is largely observed in the Batchelor regime (Tsang *et al.* 2005).

Here, we develop a general aggregation theory for scalar mixing in smooth, two-dimensional, and fully chaotic flows in the Batchelor regime. The theory is based on the description of the spatial clustering of advected material lines, and its correlation with local elongation rates. The theory allows describing the asymptotic evolution of the scalar pdf and its moments at any Péclet number based on the sole knowledge of Lagrangian stretching statistics and fractal dimensions of the advective material lines. It may be generalized to a wider range of flows and boundary conditions.

The paper is organized as follows: in the first section, we recall important concepts and variables pertaining to Lagrangian stretching and aggregation frameworks. In the second section, we present the two-dimensional incompressible chaotic flows used to illustrate and validate the general aggregation theory, and their numerical resolution. In the third section, we focus on the geometry of material lines advected by a chaotic flow and we derive the

evolution of the pdf of the number of advective filaments in aggregates, as well as the statistics of elongation in aggregates. In section 4, we describe how the scalar concentration pdf and its moment can be obtained from the knowledge of both the distribution of aggregate size and filaments statistics in aggregates.

2. Lagrangian stretching and aggregation

2.1. Stretching and dilution

We focus on smooth, two-dimensional, incompressible and time-varying flows, for which there exists two Lyapunov exponents of opposite signs. Advection thus creates elongated one-dimensional structures, called lamella or filament, that are the backbone of scalar mixing.

The temporal evolution of single scalar filaments is trackable in a Lagrangian frame with a coordinate system (x, y) advected with the flow and aligned with the directions of compression (x) and elongation (y) (Ranz 1979; Villiermaux 2019). Because of their elongated shape, the concentration of lamellae is approximately constant in the y direction. Thus, $\partial_y c$ is negligible compared to $\partial_x c$, and the two-dimensional advection-diffusion problem (1.1) simplifies to a one-dimensional advection-diffusion equation

$$\partial_t c + u(x)\partial_x c = \kappa \partial_x^2 c, \quad (2.1)$$

with $u = -x\lambda(t)$ the velocity at which solute particles are compressed in the direction x and $\lambda(t) \geq 0$ the stretching rate. In two-dimensional incompressible flows, the stretching rate $\lambda(t)$ in the y -direction leads to a compression rate $-\lambda(t)$ in the x -direction. In chaotic flows, the mean stretching rate μ_λ is positive and equal to the Lyapunov exponent. We define the total lamella elongation as

$$\rho(t) = \exp\left(\int_0^t \lambda(t') dt'\right). \quad (2.2)$$

Ranz (1979) showed that Eq. (2.1) transforms to the simple diffusion equation

$$\partial_\tau c = \partial_\xi^2 c, \quad (2.3)$$

if time is rescaled by

$$\tau(t) = \frac{\kappa}{s_0^2} \int_0^t \rho(t')^2 dt', \quad (2.4)$$

and space is rescaled by $\xi = x\rho/s_0$, with s_0 the initial lamella width. For a Gaussian initial condition $c(\xi, 0) = \theta_0 \exp(-\xi^2)$, the solution of (2.3) is

$$c(\xi, \tau) = \frac{\theta_0}{\sqrt{1+4\tau}} \exp(-(\xi/\sqrt{1+4\tau})^2). \quad (2.5)$$

Equivalently in the original Lagrangian coordinate system (x, y) ,

$$\Theta(x, t) = \theta(t) \exp(-(x/s(t))^2), \quad (2.6)$$

where θ is the maximum concentration of the lamella, following

$$\theta(t) = \frac{\theta_0}{\sqrt{1+4\tau(t)}}, \quad (2.7)$$

and s the unit lamella thickness, following

$$s(t) = \frac{s_0 \sqrt{1+4\tau(t)}}{\rho(t)}. \quad (2.8)$$

Note that the scalar mass per unit length under a lamella simplifies to

$$m(t) = \sqrt{\pi}\theta s(t) = \sqrt{\pi}s_0\theta_0\rho^{-1}(t). \quad (2.9)$$

Since in random flows, the stretching rate is a random variable of time, the elongation of lamellae and the rescaled time are also randomly distributed. An approximation of the statistics of τ was proposed (Meunier & Villermaux 2010; Lester *et al.* 2016) as

$$\tau \approx \frac{\kappa}{2s_0^2} \frac{t}{\log \rho} (\rho^2 - 1), \quad (2.10)$$

recognising the fact that the last stretching events have a predominant weight in the stochastic integral (2.4). At large time, $\rho \gg 1$ and $\log \rho/t \rightarrow \mu_\lambda$. Note that the notation

$$\mu_\bullet = \langle \bullet \rangle \quad (2.11)$$

is used through the paper for a mean quantity. Thus,

$$\tau \rightarrow \frac{\kappa}{2\mu_\lambda s_0^2} \rho^2 = \frac{1}{4} \left(\frac{s_B}{s_0} \rho \right)^2, \quad (2.12)$$

with the so-called Batchelor scale

$$s_B = \sqrt{2\kappa/\mu_\lambda}. \quad (2.13)$$

Note that, in his seminal paper, Batchelor (1959) uses the mean turbulent strain rate instead of the Lyapunov exponent μ_λ to quantify fluid stretching. Thus, filaments dilute at large times, with a peak concentration following

$$\theta(t) \rightarrow \frac{\theta_0 s_0}{s_B} \rho^{-1}(t) \quad (2.14)$$

while their thickness tends to the Batchelor scale $s \rightarrow s_B$. In contrast, the length of filaments grows as

$$L(t) = \ell_0 \mu_\rho(t), \quad (2.15)$$

where ℓ_0 is the initial filament length. Eq. (2.14) shows that the concentration of single diffusing filaments is inversely proportional to their elongation. Thus, describing the advective stretching statistics is sufficient to describe the mixing of passive scalar. Indeed, the spatial variance of an elongated material line in a flow domain of area \mathcal{A} can be obtained by integration of the lamellar concentration (Eq. (2.14)) squared along the filament path (Meunier & Villermaux 2010), giving

$$\sigma_c^2 \sim \frac{1}{\mathcal{A}} L(t) \mu_\rho^{-2} = \frac{1}{\mathcal{A}} \mu_\rho^{-1}. \quad (2.16)$$

Assuming a normal distribution of stretching with mean $\mu_\lambda t$ and variance $\sigma_\lambda^2 t$, the scalar variance decays can be estimated from the stretching statistics. For flows with moderate stretching variability, where $\sigma_\lambda^2 \leq \mu_\lambda$,

$$\sigma_c^2 \sim \exp\left(-(\mu_\lambda - \sigma_\lambda^2/2)t\right). \quad (2.17)$$

In contrast, for flows with larger stretching variability where $\sigma_\lambda^2 \geq \mu_\lambda$, the value of μ_ρ^{-1} is entirely controlled by small elongations with $\rho \leq 1$ (Balkovsky & Fouxon 1999). In that case, $\mu_\rho^{-1} \sim \exp(-\mu_\lambda^2/(2\sigma_\lambda^2)t)$.

It is important to note that the Lagrangian stretching approximation is correct in the limit of one dimensional filaments, that is when the curvature radius is much larger than

the diffusing filament width s_B . In bounded flow domains, there exist regions where high curvature develop (Tang & Boozer 1996) which are known (Thiffeault 2004) to be associated with weak stretching rates (low elongations) and thus low mixing (high concentrations). This questions the ability of the Lagrangian stretching framework to capture the tails of the scalar concentration pdf. However, at small κ (small s_B), the impact of these regions on global mixing rates should remain limited. This is confirmed by the good agreement of the Lagrangian stretching theory with observed mixing rates (Haynes & Vanneste 2005).

2.2. Aggregation

The production of curvature tends to produce folds in the material line (Fig. 1b). The distance between separated parts of the elongated material line is thus reduced exponentially via fluid compression. This mechanism creates a highly foliated structure at late time (Fig. 1a). Individual filaments are thus no longer isolated, and start to coalesce on length scales comparable to their width s_B . This so-called aggregation regime (Villermaux & Duplat 2003) has two properties.

First, filaments tend to accumulate locally due to exponential flow compression. *Bundles* of aggregated lamellae are thus formed by individual filaments sharing the same diffusive neighbourhood of size $\sim s_B$. The time at which aggregation initiates is when the total area of a lamella of length $L(t)$ and width s_B is greater than the available area of the flow domain \mathcal{A} (Garrett 1983), e.g.

$$L(t)s_B \gtrsim \mathcal{A}, \quad (2.18)$$

The mean number of lamella n in each bundles is thus

$$\mu_n(t) \sim \frac{L(t)s_B}{\mathcal{A}}. \quad (2.19)$$

Assuming a constant stretching rate λ , the length of lamella is $L(t) = \ell_0 \exp(\lambda t)$, the coalescence time t_c at which Eq. 2.18 is first fulfilled is

$$t_c \sim \frac{1}{\lambda} \log \left(\frac{\mathcal{A}}{\ell_0 s_B} \right). \quad (2.20)$$

Second, the linearity of the advection-diffusion equation implies that scalar concentration fields can be decomposed into a sum over the concentration profiles of solitary lamellae (Le Borgne *et al.* 2017). The scalar concentration c at a given position can be constructed as the sum of concentrations θ_i of individual lamella i (and defined by Eq. (2.14)) present in a small neighborhood around this position, of size s_a comparable to the asymptotical size of lamella, s_B , that is

$$c(t) \sim \sum_{i=1}^{n(t)} \theta_i(t) \sim \sum_{i=1}^{n(t)} \rho_i^{-1}(t), \quad (2.21)$$

where the asymptotic relation between θ and ρ (Eq. (2.14)) was used. Through Eq. (2.21), the aggregation process offers an appealing way to model the statistics of the scalar concentration field c via the knowledge of the aggregated number of filaments n at the aggregation+ scale s_a , their elongations ρ_i , and the possible correlations between these two variable.

Assuming no correlations between n and ρ_i , and among ρ_i , leads to a *random* aggregation scenario. The scalar concentration c in a bundle is thus formed by the sum of independent and identically distributed random variables, following the solitary filament concentration pdf. The scalar concentration pdf, $P_c(c, t)$, thus results from the n -convolution of the isolated lamella concentration pdf $P_{1/\rho}(\rho^{-1}, t)$, with the mean number of aggregations μ_n given by Eq. (2.19) (Duplat & Villermaux 2008). If $P_{1/\rho}$ is exponential or gamma distributed,

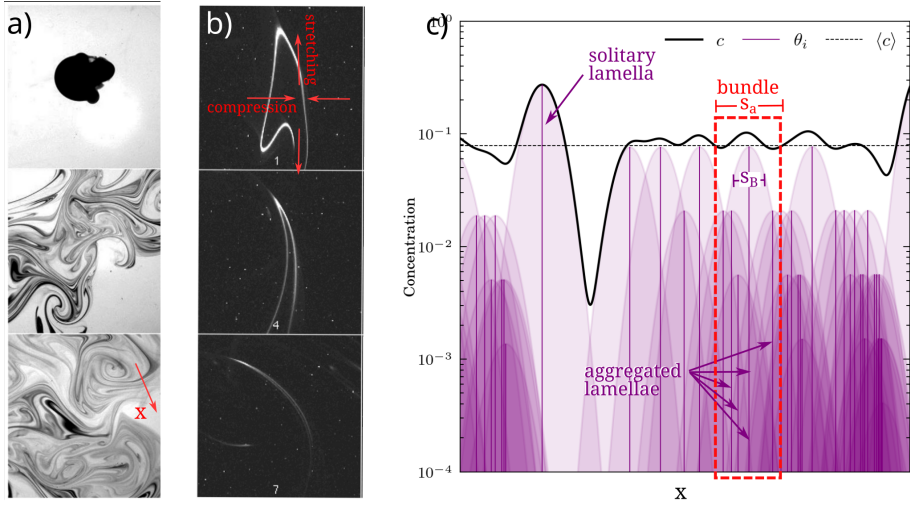


Figure 1: a. Mixing of a diffusive scalar by a random stirring protocol (time sequence top to bottom), evidencing the apparition of stretched scalar filaments (adapted from Villermaux (2012)). b. Blow up on the coalescence of neighbouring filaments under the action of compression (adapted from Duplat & Villermaux (2008)) c. Concentration profile of a scalar field showing the coexistence of solitary filaments and bundles of filaments. The scalar concentration c is obtained by the superposition of individual lamellae in a bundle of size s_a . All lamellae have a Gaussian shape with decaying maximum concentration θ_i (Eq. (2.14)) and width tending to s_B .

then P_c is a gamma distribution. Note that if $P_{1/\rho}$ is log-normal, the n -convolution pdf is not explicit, although its moments are given by the central limit theorem (Schwartz & Yeh 1982). This random conjecture was shown (Duplat & Villermaux 2008) to correctly describe mixing in turbulent flows, for which the velocity cascade over a large range of scales favor the decorrelation of filament stretching histories.

Below the characteristic velocity length scale (the Batchelor regime), however, filament aggregation seems not to obey completely random dynamics. To see that, it is useful to consider the decay of scalar variance. In the random hypothesis, by the central limit theorem, scalar variance decays as the inverse of the aggregation number, that is, the inverse of the material length (Eq. (2.19)):

$$\sigma_c^2 = \frac{\mu_c^2}{\mu_n} \sim 1/L(t). \quad (2.22)$$

Assuming a normal distribution of stretching rates, $L \sim \exp((\mu_\lambda + \sigma_\lambda^2/2)t)$ and thus the asymptotic scalar variance decay exponent is $\mu_\lambda + \sigma_\lambda^2/2$, larger than the decay exponent of solitary strips ($\mu_\lambda - \sigma_\lambda^2/2$, Eq. (2.17)). This result is in contradiction with observations suggesting the same decay exponent before and after aggregation time in the Batchelor regime (Fereday *et al.* 2002; Tsang *et al.* 2005).

We attribute this failure to the existence of correlations in the aggregation process below the characteristic velocity length scale. Indeed, in incompressible flows, lamella elongation is always balanced with transverse compression (Fig. 1b), which attracts neighbouring lamella onto each-other. Thus, highly stretched lamella tend to be highly aggregated. Conversely, weakly stretched lamella have also experienced little compression, thus remaining isolated from the bulk and their evolution well described by the isolated lamellar theory. Since these lamella bears high concentration levels, they must dominate the statistics of scalar fluctuations

at late time. Such correlations may explain why the Lagrangian stretching prediction for the scalar dissipation remains accurate long after aggregation time.

Evidence of correlated aggregation was also observed experimentally during the chaotic mixing of two dye blobs (Duplat *et al.* 2010). If injected in a concentric manner the blobs locally experience similar stretching rates and aggregate in a correlated manner. In contrast, when placed at a certain distance from each other (larger than the characteristic length scale of the velocity field), their concentrations obey random aggregation rules. This observation suggests that stretching and aggregation are strongly correlated below the characteristic velocity length scale while they become uncorrelated above this scale.

The remaining of the paper aims at establishing the laws governing correlated aggregation for scalar mixing by smooth chaotic flows, and at deducing their impact on the evolution of scalar concentration pdf.

3. Numerical simulation of synthetic chaotic flows

We focus on scalar mixing in the so-called Batchelor regime (Haynes & Vanneste 2005) where the velocity field is smooth and present a single length scale, much greater than the typical scalar fluctuation scale. The domain size and the velocity length scale are of comparable magnitude, $\mathcal{L} \sim \mathcal{L}_v \sim 1$; the so-called “local” mixing regime described in Haynes & Vanneste (2005). Thus, no scalar gradients can persist at scales larger than the velocity scale.

To illustrate the geometrical features of aggregation, we use two synthetic chaotic transformations that complies with these conditions, namely the baker map and the random sine flow (Fig. 2). These are simple sequential advective maps that have been widely used to investigate the properties of chaos (Finn & Ott 1988; Ott & Antonsen Jr 1989; Tsang *et al.* 2005; Giona *et al.* 2001; Meunier & Villiermaux 2010, 2022). We recall their definitions below.

3.1. Incompressible baker map

The incompressible baker map (Ott & Antonsen Jr 1989; Wonhas & Vassilicos 2002) is a discontinuous transformation that operates on a two-dimensional periodic domain $[0, 1] \times [0, 1]$. The transformation writes

$$x_{t+1} = \begin{cases} ax_t & \text{if } y_t < a \\ 1 - (1 - a)x_t & \text{if } y_t > a \end{cases},$$

$$y_{t+1} = \begin{cases} y_t/a & \text{if } y_t < a \\ (1 - y_t)/(1 - a) & \text{if } y_t > a \end{cases},$$

where $a \in [0, 0.5]$ is a parameter controlling the heterogeneity of the map. A visual sketch of the map operation is plotted in (Fig. 2a).

An advantage of the baker map is that purely vertical scalar patterns (for which $c(x, y) = f(x)$) remain one-dimensional after application of the map, thus simplifying the problem to a single dimension. This simplicity allows for the analytical derivation of many features of the map, as we will show later. Another advantage is that it is possible to explore a wide range of stretching heterogeneity by varying a between 0 and 0.5. Indeed, the first two moments of stretching rate in the baker map are

$$\mu_\lambda/t = -a \log(a) - (1 - a) \log(1 - a), \quad (3.1)$$

$$\sigma_\lambda^2/t = a(1 - a)(\log(1 - a) - \log(a))^2. \quad (3.2)$$

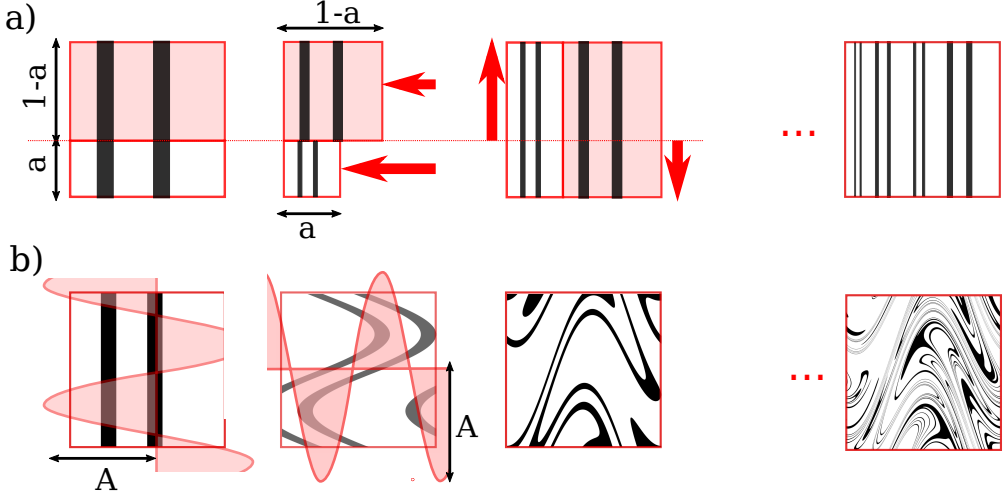


Figure 2: a) Transformations operated by the incompressible baker map with parameter a . First, the domain is cut horizontally at $y = a$, where a is a constant between 0 and 0.5. Uniform fluid compression operate on the domain parts $y < a$ and $y > a$ with a and $1 - a$ respectively. Then, vertical stretching occurs with a factor $1 - a$ and a in these two regions, preserving the total area. b) Transformations operated by the sine flow with amplitude A . The flow is an alternation of horizontal and vertical sinusoidal velocity waves with amplitude A and period 2π . Random phases are chosen at each time periods so that the flow is fully chaotic.

Thus, for $a = 0.01$, $\sigma_\lambda^2/\mu_\lambda = 3.7$ while for $a = 0.49$, $\sigma_\lambda^2/\mu_\lambda = 5.7 \cdot 10^{-4}$. It is important to note that this map involves discontinuous transformations, or “cuts”, that are absent in continuous flows such as turbulence but are common in flows through porous media (Lester *et al.* 2013). This map also prevents the formation of folds and cusps, where the one-dimensional hypothesis of the Lagrangian stretching framework is violated. The correspondence between Eq. 1.1 and Eq. 2.1 is thus exact in this map.

3.2. Random sine flow

The random sine flow (Pierrehumbert 1994; Haynes & Vanneste 2005) is a continuous transformation operating on a periodic domain $[0, 1] \times [0, 1]$ (Fig. 2b). The flow is periodic in time and space and reads for a given time period t

$$\begin{aligned}
 y_{t'+\delta t} &= y_{t'} + A\delta t \begin{cases} \sin(2\pi x'_t + \phi_t) & \text{for } t < t' < t + 1/2, \\ 0 & \text{for } t + 1/2 < t' < t + 1 \end{cases} , \\
 x_{t'+\delta t} &= x_{t'} + A\delta t \begin{cases} 0 & \text{for } t < t' < t + 1/2, \\ \sin(2\pi y'_t + \psi_t) & \text{for } t + 1/2 < t' < t + 1 \end{cases} ,
 \end{aligned}$$

where the amplitude A is a positive constant and ϕ_t, ψ_t are random phases that change at each time period t , and δt the time step. The flow velocity having a single component, incompressibility is enforced. Scalar transport is continuous and considered on a periodic domain $[0, 1] \times [0, 1]$, ensuring a *local* control of mixing rates (Haynes & Vanneste 2005).

As most random chaotic flows, the elongation of material lines in sine flows approximately follows a log-normal distribution with parameters $\mu_\lambda t$ and $\sigma_\lambda^2 t$ that depend on the amplitude A . The stretching heterogeneity is much less variable than in the baker map, with ratio $\sigma_\lambda^2/\mu_\lambda$

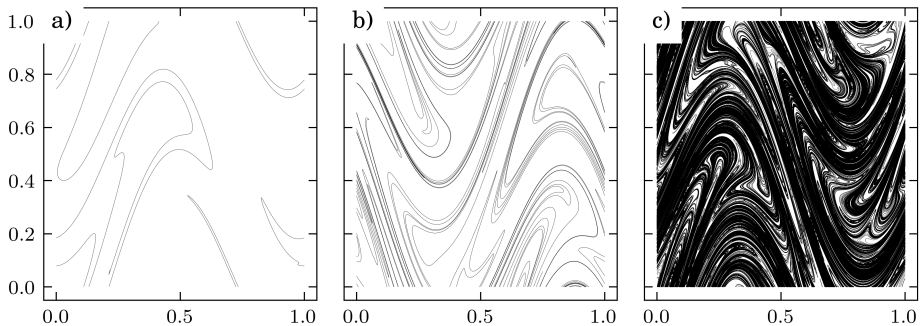


Figure 3: Advection of a material filament in the sine flow with $A = 0.8$, for a) $t = 3$ b) $t = 5$ and c) $t = 10$.

ranging from 1 when $A \rightarrow 0$ to $\sigma_\lambda^2/\mu_\lambda \approx 0.6$ for $A = 1.8$. The stretching statistics of random sine flows can be found in Meunier & Villiermaux (2022). In Appendix A, we recall useful results concerning the distribution of filament elongation and its moments in the sine flow and the baker map.

3.3. Numerical methods

The hypothesis used through the paper is that the concentration field obeying Eq. (1.1) is well approximated by a local summation over elementary lamellar concentrations, each of them individually following Eq. (2.1). This implies that the statistics of concentrations and their temporal evolution can in principle be inferred from the statistics of lamella elongation and aggregation. Thus, instead of directly solving the two-dimensional advection-diffusion equation (Eq. (1.1)), our approach consists in computing elongation of a deforming Lagrangian support, advected by the flow (Fig. 3).

Numerically, we advect a material line of initial length ℓ_0 in the velocity field. In practice, the material line is defined by a series of particles \mathbf{x}_i linked by segments. In the alternated random sine wave, the position of particles is tracked through time t via an explicit Euler scheme (Fig. 3). The particles have constant velocities during a time step $dt = 1/2$, so that this scheme is exact. The local elongation of segments is estimated as

$$\rho_i(t) = \rho_i(t - dt) \frac{\|\mathbf{x}_i(t + dt) - \mathbf{x}_{i+1}(t + dt)\|}{\|\mathbf{x}_i(t) - \mathbf{x}_{i+1}(t)\|}. \quad (3.3)$$

The material line is refined after each time step to maintain a maximum local distance between points of $dx \leq 10^{-3}$.

In the baker map, we start by a single filament aligned with the y direction, so that we only need to track its coordinate x . Each operation of the map doubles the number of filaments, with the first half being elongated by a factor $1/a$ and the second half by a factor $1/(1-a)$. We thus keep track of the growing number of filament positions x_i and their elongations ρ_i .

The elongated and folded filament is tracked up to the advection time where the total length is $L = 10^7 \ell_0$, limit corresponding to our computer memory. Local elongation of the advected material line can then be used to compute its local concentration, via Eq. (2.14). Aggregated scalar field can then be estimated by a local summation of individual lamellar concentration, via Eq. (2.21).

3.4. Reconstruction of scalar fields

As shown by Meunier & Villermaux (2010), it is possible to reconstruct the aggregated scalar field via the superposition of elementary lamella, represented as Gaussian ellipsoids of short axis s , that swipe along the advected material line. This reconstruction is exact in the Baker map since no cusps are forming. In the sine flow, it is only approximate in the regions of high curvature, where diffusion is genuinely two-dimensional.

Here, we take an alternative reconstruction approach, which has the advantage of allowing analytical treatment. At late time, lamella widths tend to s_B (Eq. (2.13)), which is the minimum scale of fluctuations of the scalar field (Batchelor 1959). Thus, we construct the aggregated scalar field by binning lamella concentrations on a regular grid of size $s_a \sim s_B$. Consider a box of surface s_a^2 centred in position \mathbf{x} , the aggregated concentration level in this box can be constructed from the sum of the masses per unit length m_i of the $n(\mathbf{x})$ individual lamellae of length ℓ_i present in this box

$$c(\mathbf{x}) \approx \frac{1}{s_a^2} \sum_{i=1}^{n(\mathbf{x})} s_a m_i = \frac{\sqrt{\pi} \theta_0 s_0}{s_a} \sum_{i=1}^{n(\mathbf{x})} \rho_i^{-1}. \quad (3.4)$$

where we used Eq. (2.9) for the evolution of the solute mass per unit length carried by an individual lamella at a given location. Eq. (3.4) forms the base of the statistical description of aggregation intended in this paper.

In practice, we choose

$$s_a = \sqrt{2\pi} s_B, \quad (3.5)$$

for the variance of the regular grid reconstruction to match the variance of the true field (i.e., the one obtained by aggregating Gaussian lamellae). The factor $\sqrt{2\pi}$ is obtained so that both reconstruction methods provide the same mean-squared concentration in the case of a single lamella.

Note that the aggregated concentration field can be deduced at various Péclet numbers by varying the aggregation scale s_a (Eq. (3.5)), without recomputing the advective filament position. We define the Péclet number as the ratio of diffusive to stretching time scales, e.g.,

$$\text{Pe} = \mu_\lambda \mathcal{L}_v^2 / \kappa. \quad (3.6)$$

Through Eq. (2.13), $s_B = \mathcal{L}_v \sqrt{2/\text{Pe}}$ and thus $s_a = 2\sqrt{\pi} \mathcal{L}_v / \text{Pe}$.

This regular grid approximation of the aggregated scalar field disregards the exact Gaussian shape of lamellar concentrations and the variations of their width s (Eq. (2.5)). However, classical box counting methods and fractal dimensions can be used to describe the geometrical and statistical features of the aggregated scalar field. Our goal is to describe the joint statistics of the variables ρ_i and n arising in Eq. (3.4), to infer the statistics of c .

The approximation (3.4) is compared to direct numerical simulations (DNS) of the advection-diffusion equation for different Péclet numbers in Fig. 4. DNS is obtained with the spectral method described in Meunier & Villermaux (2022), with a 2048^2 grid and a time step of 0.1. There is a good qualitative match between the aggregated field and the DNS, match confirmed by comparing the distributions of concentrations. Thus, we conclude that the construction of the aggregated scalar field via Eq. (3.4) is able to capture the essential statistical features of the two-dimensional advection-diffusion problem, and offers a convenient way to explore its statistics.

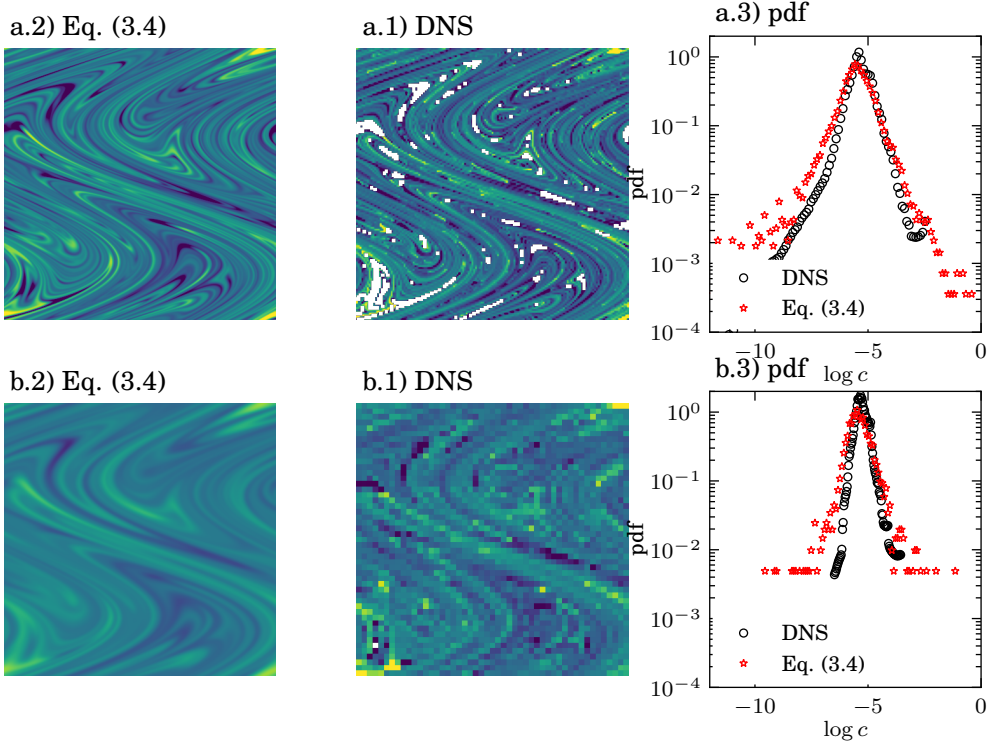


Figure 4: Comparison of log-concentration fields obtained at time $t = 10$ (fully aggregated regime) .1), with the aggregation framework (Eq (3.4)), .2) with Direct Numerical Simulation of Eq. (1.1) and 3.) their pdf. The comparison is made for the sine flow ($A = 0.8$) for two Péclet numbers, corresponding to $s_a = 1/150$ (a.) and $s_a = 1/50$ (b.)

4. Clustering properties of advected material lines

In incompressible flows, the stretching of material elements by velocity gradients is compensated by transverse compression. Compression causes distances between lamellar elements to decrease exponentially over time. Smaller and smaller scales are thus continuously produced by flow compression. Furthermore, in smooth chaotic flows, the typical scale of variation of velocity gradients is fixed and produces a heterogeneous stretching field for material lines. Dense (black) or diluted (white) regions of material lines are thus created at large scale in the chaotic flow (Fig. 5). Such heterogeneous structures then cascade to smaller scales under the action of net compression, thus creating a fractal set of one-dimensional objects (lines) clustered around their transverse direction. In two-dimensional incompressible flows, the Hausdorff dimension of this fractal set is necessarily $D_0 = 2$, as per the Kaplan-York result (Farmer *et al.* 1983). Higher order dimensions can be smaller than 2 if stretching is heterogeneous. To illustrate this, let us define a normalised measure p_k with $k = 1 \dots N$ defining a regular grid of bin size $\epsilon = \mathcal{L}/N$, where \mathcal{L} is the domain size. For instance, p_k may be defined as the local density of lamella in the bin, e.g. $p_k = n_k/n$ where n is the total number of lamella.

The fractal dimension of order q of the measure p is obtained with (Grassberger 1983):

$$D_q - 1 = \lim_{\epsilon \rightarrow 0} \frac{1}{q-1} \frac{\log I_q(\epsilon)}{\log \epsilon}, \quad I_q(\epsilon) \equiv \sum_k^{N=\mathcal{L}/\epsilon} p_k^q, \quad (4.1)$$

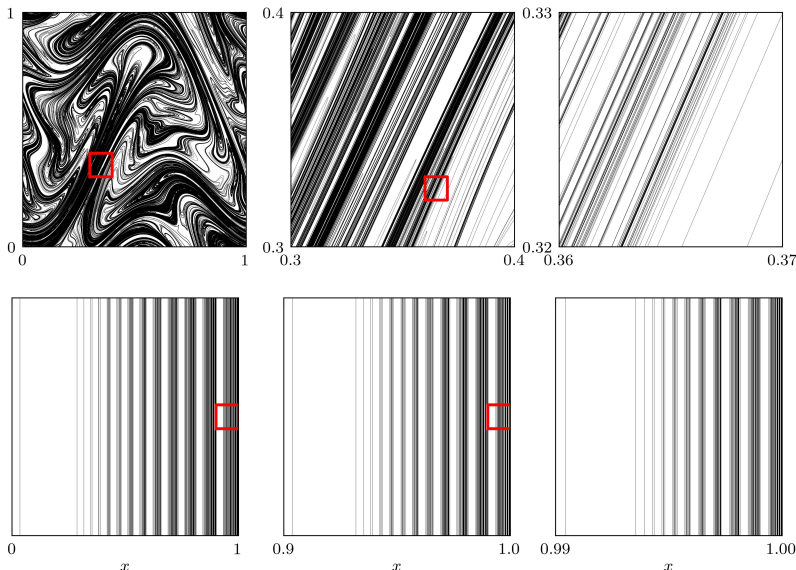


Figure 5: Fractal geometry of material lines in (top) the sine flow ($A = 0.8$) and (bottom) the baker map ($a = 0.1$) observed at different scales. The red square indicates the area selected for zooming.

where the subtraction of 1 on the left hand side accounts for the counting of one-dimensional structures (lamellae) in a two-dimensional domain. This definition implies the following spatial scaling of the integral of the measure:

$$I_q(\epsilon) \sim \epsilon^{(q-1)(D_q-1)}. \quad (4.2)$$

In simple flows such as the baker map, D_q can be obtained (Finn & Ott 1988) by observing the similarity properties of the map, which transfer at small scales the heterogeneity of the measure produced at large scales by a single operation of the map. Characterising the result of one elementary operation of map on the measure thus also informs about the spectrum of fractal dimensions.

We consider the measure of the local number of lamella in bin k , $p_k = n_k/n$. As shown in Fig. 2a, an operation of the baker map doubles the total number of these lamellae, while maintaining the same local distribution of lamellae on smaller bins of sizes $a\epsilon$ for $x < a$ and $(1-a)\epsilon$ for $x > a$. This similarity allows one to compute the first fractal dimension explicitly (see Appendix B and Finn & Ott (1988)),

$$D_0 = 2, \quad D_1 = 1 + \frac{2 \log 2}{\log(a^{-1} + (1-a)^{-1})}. \quad (4.3)$$

For random flows such as the sine flow, Ott & Antonsen Jr (1989) argue that there exists a general relationship between stretching rate statistics and fractal dimensions as $D_q = f_q(\sigma_\lambda^2, \mu_\lambda)$, although a closed-form solution is not always as trivial as for the baker map. We show in Fig. 6 that the ratio $\sigma_\lambda^2/\mu_\lambda$ is directly related to the fractal dimension D_1 . This suggests that the fractal clustering of material lines is closely linked to the large-scale heterogeneity of stretching rates. Since the flow is smooth, the heterogeneity created at large scales cascades to smaller scales, conserving its geometrical structure and creating a fractal geometry.

As suggested by Figure. 6, the function f_1 is different for baker map and the sine flow.

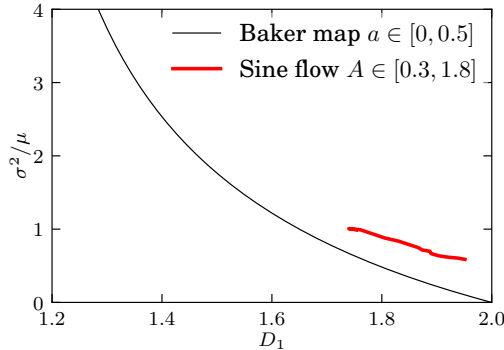


Figure 6: Relation between stretching rate mean μ_λ and variance σ_λ^2 and fractal dimension D_1 in the baker map and sine flow with varying parameters a and A .

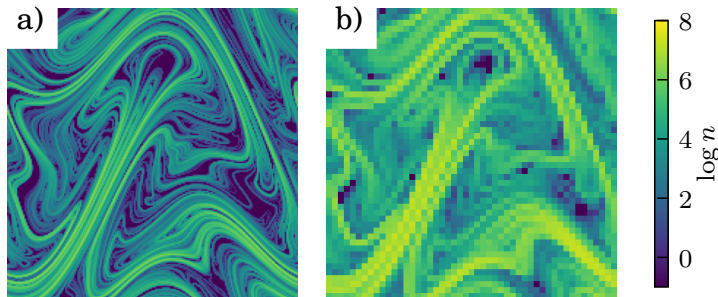


Figure 7: Spatial distribution of the number n of lamella in bundles defined by a regular grid of size a) $s_a = 1/200$ and b) $s_a = 1/50$, in the sine flow with parameter $A = 0.5$.

Indeed, the ratio $\sigma_\lambda^2/\mu_\lambda$ tends to a positive constant in the sine flow when $A \rightarrow \infty$, while $\sigma_\lambda^2/\mu_\lambda \rightarrow 0$ in the baker map when $a \rightarrow 0.5$. This finite limit comes from the fact that the sine flow is a continuous transformation with no cutting and thus does not tend to a uniform stretching rate. In the contrary, when $A \rightarrow 0$, $\sigma_\lambda^2/\mu_\lambda \rightarrow 1$ which is a maximum bound for the ratio in the sine flow (Meunier & Villermaux 2022), thus limiting the possible range of fractal dimensions produced by continuous chaotic flows, compared to discontinuous maps.

4.1. Spatial distribution of n

The spatial distribution of the number n of lamella per bin size \mathcal{A} (Fig. 7) can be obtained as follows. Comparing the mean area occupied by a filament of length $L(t)$ and aggregation scale s_a to the domain surface \mathcal{A} , we get an estimate of the mean number of lamellae μ_n in bundles

$$\mu_n \sim L(t)s_a/\mathcal{A}. \quad (4.4)$$

Higher moments can be obtained from a study of the fractal structure of material lines. To this end, we consider the spatial measure corresponding to the local number of lamellae in each bundle:

$$p_k \equiv \frac{n_k}{\sum_k n_k} \quad (4.5)$$

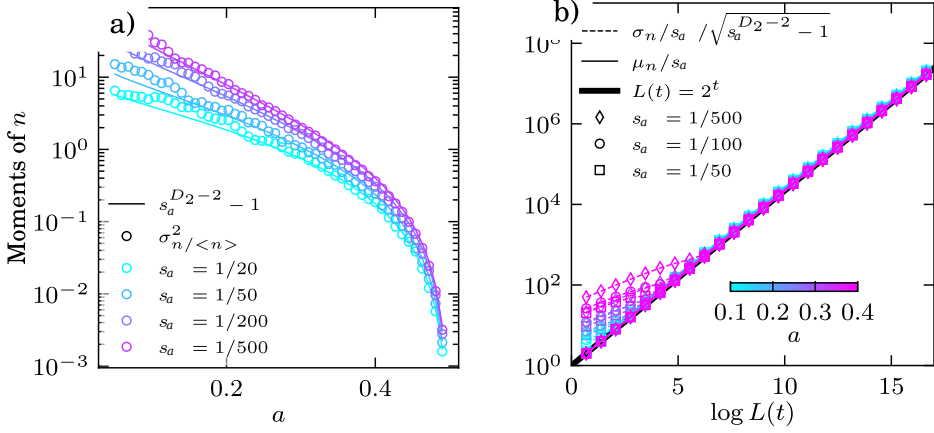


Figure 8: a) Scaling of the spatial variance of $\log n$ as a function of a in the baker map and theoretical prediction, Eq. (4.10). b) First two moments of P_n through time compared to theoretical predictions, Eqs. (4.4) and (4.11) in the baker map ($\mathcal{A} = 1$).

The Renyi definition (Grassberger 1983) of the fractal dimension of order 2 of this measure is

$$D_2 - 1 \approx \frac{\log \sum_k p_k^2}{\log s_a}, \quad (4.6)$$

assuming $s_a \rightarrow 0$. Replacing Eq. (4.5) in the last expression provides

$$\sum_k \left(\frac{n_k}{\sum_k n_k} \right)^2 = s_a^{D_2-1}. \quad (4.7)$$

Since $\sum_k n_k = N\mu_n$ we have

$$\sum_i \left(\frac{n_k}{\sum_k n_k} \right)^2 = \frac{1}{N} \langle (n/\mu_n)^2 \rangle, \quad (4.8)$$

with $N \approx \sqrt{\mathcal{A}}/s_a$ the number of bundles in the flow domain. Since

$$\sigma_{n/\mu_n}^2 = \langle (n/\mu_n)^2 \rangle - \langle n/\mu_n \rangle^2, \quad (4.9)$$

then,

$$\sigma_{n/\mu_n}^2 = \sqrt{\mathcal{A}} s_a^{D_2-2} - 1. \quad (4.10)$$

Thus the variance of n/μ_n reaches a constant at asymptotic times, which is given by the fractal dimension of order 2. The spatial variance of n is then

$$\sigma_n^2 = \mu_n^2 \left(\sqrt{\mathcal{A}} s_a^{D_2-2} - 1 \right) \quad (4.11)$$

The predictions of Eqs. (4.4)-(4.11) are plotted against time in Fig. 8 and Fig. 9 showing good agreement with simulations for a large range of Batchelor scales s_a and flow heterogeneity, characterized by the parameters a for the Baker map and A for the sine flow. Higher moments of n can be obtained with similar scaling arguments and linked to fractal dimension of higher order. This is however out of the scope of the present study.

Instead, we observed that the pdf of lamella aggregation number $P_n(n)$ is well fitted by a

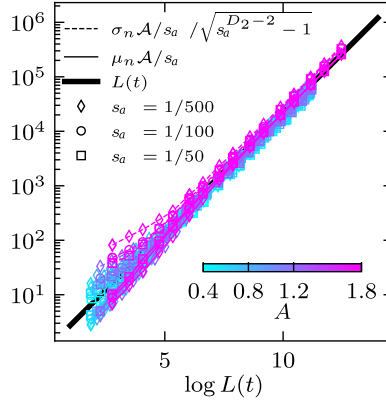


Figure 9: First two moments of P_n through time compared to theoretical predictions, Eqs. (4.4) and (4.11) in the sine flow ($\mathcal{A} = 1$).

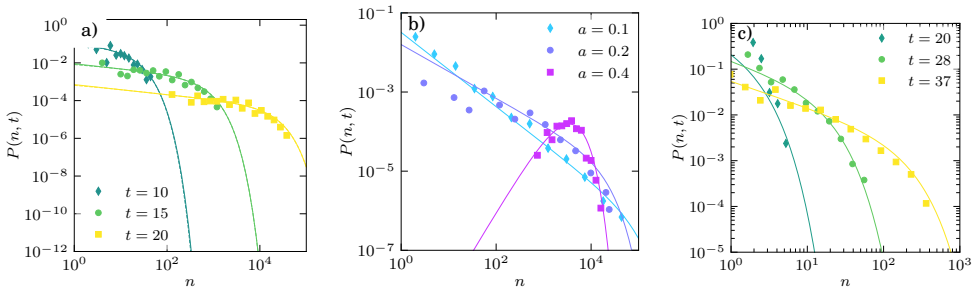


Figure 10: $P(n, t)$ for the baker map and sine flow for $s_a = 1/100$. Solid lines stand for the gamma pdf with theoretical moments given by Eq. (4.14) and dots stand for numerical simulations. a) baker map $a = 0.3$ and variable t . b) baker map for $t = 20$ and variable a . c) sine flow for $s_a = 1/100$ and $A = 0.4$.

Gamma distribution (Fig. 10):

$$P_n(n) = \frac{1}{\Gamma(k_n)\theta_n^{k_n}} n^{k_n-1} \exp(-n/\theta_n), \quad (4.12)$$

with $n \geq 0$ and k_n, θ_n defined by the moments of the distribution of n :

$$k_n = \left(\sqrt{\mathcal{A}s_a^{D_2-2}} - 1 \right)^{-1}, \quad (4.13)$$

$$\theta_n = \mu_n(t) \left(\sqrt{\mathcal{A}s_a^{D_2-2}} - 1 \right), \quad (4.14)$$

with $\mu_n = L(t)\mathcal{A}/s_a$. Note that the gamma distribution yields a power law distribution at small n with exponent $k_n - 1$ going from -1 to infinity with increasing D_2 . For small D_2 (strong stretching heterogeneity), a significant part of the probability is concentrated at small n , thus in non-aggregated regions of the flow. We will show later that this can affect the value of negative moments of n .

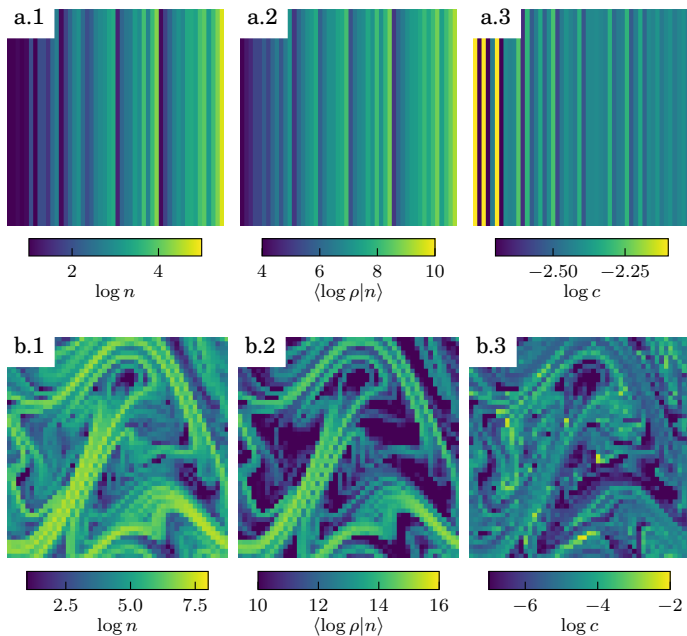


Figure 11: Simulation of aggregation statistics in baker map ($a = 0.3$) and sine flow ($A = 0.5$) for $s_a = 1/50$: .1 number of lamella n in bundles, .2 mean of log-elongation in bundles and .3 sum of lamellar concentrations in bundles.

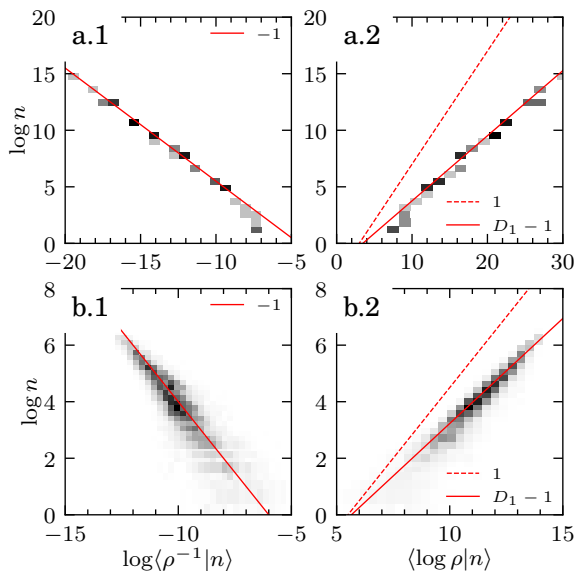


Figure 12: Joint pdf (gray scale) of the number of lamellae in a bundle of size $s_a = 1/200$ and (1) their mean inverse elongation (2) and their mean log-elongation for (a.) baker map ($a = 0.1, t = 24, D_1 = 1.57$) and (b.) sine flow ($A = 0.8, t = 10, D_1 = 1.74$). The theoretical scaling of the measure (1) and (2), given by Eq. (4.16) and (4.18) respectively, are plotted as a continuous red lines with the slope indicated in the legend. Dashed red lines are guides to the eyes.

4.2. Local correlations between n and ρ

Having precised the statistics of the bundle size n , we now explore the local statistics of lamella elongations in these bundles. To this end, we define the conditional averaging operator acting in lamellae located in the local neighbourhood of size s_a by

$$\mu_{X|n} = \frac{1}{n} \sum_{i=1}^n X_i, \quad (4.15)$$

where X is a Lagrangian variable transported by lamellae and n is the number of lamellae aggregated in the bundle. The remainder of this section is dedicated to uncovering the behaviour of conditional moments of elongation conditioned to n (e.g. $\mu_{\rho^{-a}|n}$). Section 5 will then be dedicated to deriving unconditional probabilities by averaging on the distribution of n .

We plot in Fig. 12 the joint probability $P(n, \mu_{X|n})$ obtained in the baker map and the sine flow for $X = \rho^{-1}$ and $X = \log \rho$, the inverse of elongation and the log-elongation of lamella respectively. Fig. 12 suggests that the following scaling holds in both flows:

$$\log n \sim -\log \mu_{\rho^{-1}|n}, \quad (4.16)$$

which confirms the strong correlation between the number of lamellae in aggregates and their elongation. Indeed, for large time, c must tend to the conserved average scalar concentration $c \rightarrow \mu_c$. Thus, owing to Eq. (3.4), we must have

$$n \sim 1/\mu_{\rho^{-1}|n}, \quad (4.17)$$

a scaling that we confirm numerically (Fig. 12).

Fig. 12 also suggests that

$$\log n \sim (D_1 - 1)\mu_{\log \rho|n}, \quad (4.18)$$

where D_1 is the information dimension (Ott & Antonsen Jr 1989) of the measure n , and is given by Eq. (4.3) for the baker map. Equation (4.18) can be derived analytically in the case of the baker map. Indeed, by the action of the map, the total number of lamellae increases as $\log n = t \log 2$ while the mean log-elongation of these lamellae is $\mu_{\log \rho} = t(-\log a - \log(1-a))/2$ leading to a constant ratio

$$\frac{\log n}{\mu_{\log \rho}} = \frac{2 \log 2}{\log a + \log(1-a)}, \quad (4.19)$$

which is exactly the value of $D_1 - 1$ (Eq. (4.3)). Assuming that the partition between $\log n$ and $\mu_{\log \rho}$ is preserved at small scales in each bundle, we have

$$\log n = (D_1 - 1)(\mu_{\log \rho|n} - \mu_{\log \rho_c}), \quad (4.20)$$

with $\mu_{\log \rho_c}$ a constant standing for the mean elongation at coalescence time.

The constant $\mu_{\log \rho_c}$ can be estimated by comparing the surface covered by the filament at the aggregation scale, $S = s_a \rho_c L_0$, with the domain area \mathcal{A} . The first aggregation event occurs when $S \approx \mathcal{A}$, that is when the elongation is $\rho_c \approx \mathcal{A}/(s_a \ell_0)$. Eq. (4.20) is indeed verified for baker map and sine flow with various parameters a and \mathcal{A} , with $\mu_{\log \rho_c} = -\log s_a$.

4.3. Distribution of $\log \rho$ in a bundle of size n

The two scaling laws $n \sim \mu_{\rho^{-1}|n}$ and $\log n \sim (D_1 - 1)\mu_{\log \rho|n}$ provide key information about the heterogeneity of lamella elongations inside bundles. Since the ensemble distribution of elongation $P_\rho(\rho)$ has a log-normal shape, we assume that the distribution of elongations

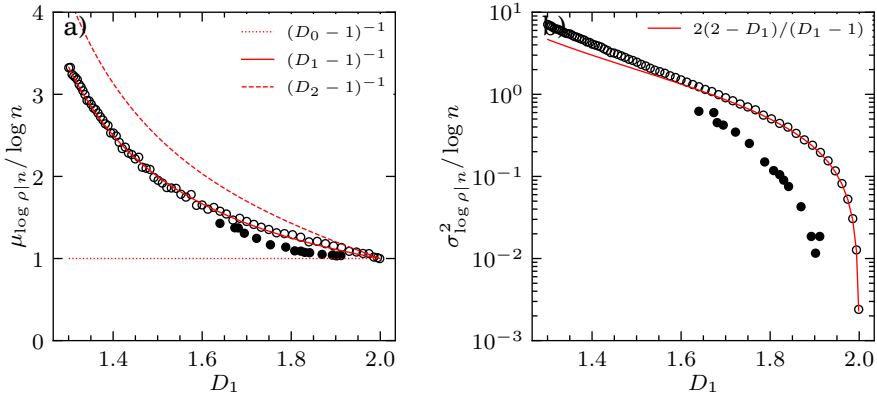


Figure 13: Scaling of the mean (a) and variance (b) of log-elongation in bundles as a function of the information dimension D_1 . Circles stands for numerical simulations in baker maps (open circles) and sine flow (filled circles). Continuous lines stands for theoretical prediction of the mean (Eq. (4.21)) and variance (Eq. (4.22)). Dashed lines are plotted to compare the mean with fractal dimension of other order.

inside bundles, denoted $P_{\rho|n}$, is also log-normally distributed. This implies that $\log \rho$ is normally distributed in bundles, with a mean

$$\mu_{\log \rho|n} \sim (D_1 - 1)^{-1} \log n. \quad (4.21)$$

Since $\log \mu_{\rho^{-1}|n} = -\mu_{\log \rho|n} + \sigma_{\log \rho|n}^2/2 \sim -\log n(x)$, the variance of log-elongation in bundles at large n must be

$$\sigma_{\log \rho|n}^2 \sim \frac{2(2 - D_1)}{D_1 - 1} \log n. \quad (4.22)$$

We report in Fig. 13 the simulated scaling $\mu_{\log \rho|n}/\log n$ and $\sigma_{\log \rho|n}^2/\log n$ obtained asymptotically at large times. When $D_1 \rightarrow 2$, $\mu_{\log \rho|n}/\log n \rightarrow 1$ while $\sigma_{\log \rho|n}^2/\log n \rightarrow 0$, meaning that bundles are formed by lamella of identical elongations. In contrast, when $D_1 \rightarrow 1$, both $\mu_{\log \rho|n}/\log n$ and $\sigma_{\log \rho|n}^2/\log n$ become infinite, while their ratio $\sigma_{\log \rho|n}^2/\mu_{\log \rho|n} = 2(2 - D_1) \rightarrow 0.5$. This limit suggests that the aggregation of lamellae remains correlated to their average elongation, although a fixed amount of stretching variability arises in bundles. A good agreement is found between theoretical prediction (Eqs. (4.21)-(4.22)) and numerical simulations of aggregation in the baker map (Fig. 13). In contrast, the theory captures only qualitatively the behaviour of the random sine flow. This may be due to the continuity of the sine flow which produces curved lamellar structures whose dimension is not exactly one-dimensional.

The stretching variability in bundles is directly linked to the heterogeneity of the chaotic flow, because of the intimate relationship existing between the fractal geometry of the material line and the stretching statistics of fluid elements (Ott & Antonsen Jr 1989). As such, it is impossible to have a single stretching rate per bundle as soon as the chaotic flow is heterogeneous and exhibits a distribution of stretching rates. The absence of stretching variability in bundles ($\sigma_{\log \rho|n}^2 = 0$) implies the uniformity of stretching at large scale ($\sigma_{\rho}^2 = 0$). This uniform case is reached when $D_1 \rightarrow D_0 = 2$, for instance, in the baker map when $a \rightarrow 0.5$. In continuous flow maps such as the sine flow, regions of high and low stretching always coexist and $\sigma_{\log \rho|n}^2 > 0$.

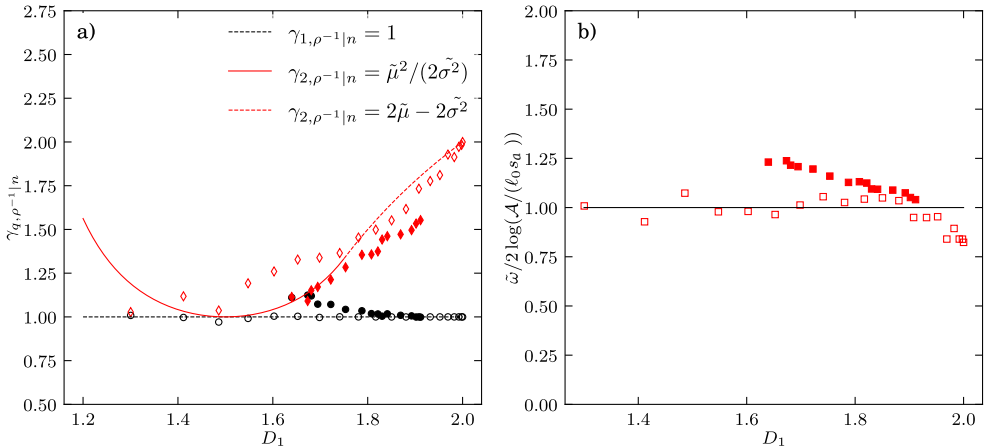


Figure 14: a) Scaling exponents of the q lamellar concentration moments in bundles (Eq. (4.23)). Numerical estimates are plotted with symbols, red diamonds for $q = 2$ and black circles for $q = 1$. Unfilled and filled symbols represents simulations in baker map and sine flow respectively. Theoretical predictions (Eq. (4.26)) are represented by lines. b) Intercept $\tilde{\omega}$ of the scaling exponent of the q lamellar concentration moments in bundles (Eq. (4.23)) in baker map (empty squares) and sine flow (filled squares) and theoretical prediction (line, Eq. (4.27)).

4.4. Moments of $1/\rho$ in a bundle of size n

Having described the first two moments of the distribution of lamella elongation in bundles (Eqs (4.21)-(4.22)), we now assume that the distribution is of log-normal shape. This choice is justified by the fact that elongation is a multiplicative process, thus usually leading to lognormal distributions (Le Borgne *et al.* 2015; Souzy *et al.* 2020). This allows us to compute the scaling of the q -moments of lamella concentrations in bundles, $\theta|n$. Owing to Eq. (2.14), we have

$$\begin{aligned}
 \mu_{\theta^q|n} &\sim \mu_{\rho^{-q}|n} \\
 &= \int_1^{\infty} \rho^{-q} P_{\rho|n}(\rho) d\rho \\
 &\approx \int_1^{\infty} e^{-(\log \rho - \mu_{\log \rho|n})^2 / (2\sigma_{\log \rho|n}^2) - q \log \rho} d\rho.
 \end{aligned} \tag{4.23}$$

The minimum bound for the integral is taken at $\rho = 1$ and not 0, taking into account the fact that lamellar structures cannot be compressed in their longitudinal direction. As a consequence, $P_{\rho|n}(\rho)$ is truncated for $\rho < 1$. Denoting $\Lambda = \log \rho / \log n$, $\tilde{\mu} = \mu_{\log \rho|n} / \log n$ and $\tilde{\sigma}^2 = \sigma_{\log \rho|n}^2 / \log n$, this expression becomes

$$\mu_{\rho^{-q}|n} \approx \int_1^{\infty} e^{H(\Lambda) \log n} d\rho, \tag{4.24}$$

with $H(\Lambda) = -(\Lambda - \tilde{\mu})^2 / (2\tilde{\sigma}^2) - q\Lambda$. For large n , the value of this integral tends to $e^{H(\Lambda^*) \log n}$ where the Λ^* is the value where H takes a maximum, that is either at $\Lambda^* = \tilde{\mu} - q\tilde{\sigma}^2$ if

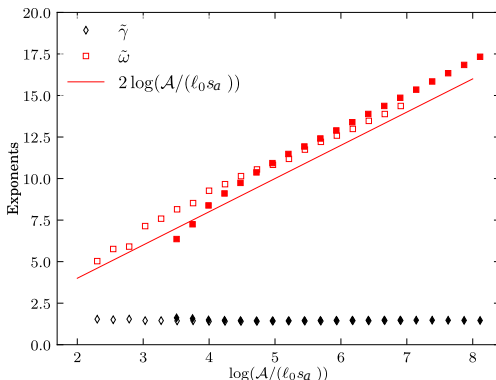


Figure 15: Dependence of $\tilde{\gamma}$ and $\tilde{\omega}$ with the aggregation scale in simulations (dots) of the baker map (empty symbols $a = 0.2$) and the sine flow (filled symbols $A = 1.2$) and comparison to theoretical prediction (Eq. (4.27)).

$\tilde{\mu} - q\tilde{\sigma}^2 > 0$, or $\Lambda^* = 0$ otherwise. Thus,

$$\log \mu_{\rho^{-q}|n} \approx -(\gamma_{q,\rho^{-1}|n} \log n + \omega_{q,\rho^{-1}|n}) \quad (4.25)$$

$$\text{with } \begin{cases} \gamma_{q,\rho^{-1}|n} = q\tilde{\mu} - q^2\tilde{\sigma}^2/2 & \text{if } \tilde{\mu} > q\tilde{\sigma}^2, \\ \gamma_{q,\rho^{-1}|n} = \tilde{\mu}^2/(2\tilde{\sigma}^2) & \text{if } \tilde{\mu} \leq q\tilde{\sigma}^2, \end{cases}$$

and $\omega_{q,\rho^{-1}|n} = q \log(\mathcal{A}/(s_a \ell_0))$ a constant. In particular, we are interested in the exponent $q = 2$ which is useful to describe fluctuations around the mean. We have

$$\tilde{\gamma} \equiv \gamma_{2,\rho^{-1}|n} = \begin{cases} 2\tilde{\mu} - 2\tilde{\sigma}^2 & \text{if } \tilde{\mu} > 2\tilde{\sigma}^2 \\ \tilde{\mu}^2/(2\tilde{\sigma}^2) & \text{if } \tilde{\mu} \leq 2\tilde{\sigma}^2 \end{cases} \quad (4.26)$$

The predicted dependence of $\tilde{\gamma}$ upon D_1 is reproduced in Fig. 14. $\tilde{\gamma}$ is bounded between 2 (for $D_1 \rightarrow 2$) and 1 for $D_1 \approx 1.5$. The prediction agrees reasonably well with numerical simulations of the baker map and sine flow (Fig. 14). The small discrepancies can be attributed to deviations from log-normally distributed elongation in bundles. We also verify numerically that $\tilde{\omega} \equiv \omega_{2,\rho^{-1}|n}$ is independent of D_1 (Fig. 14b). In Fig. 15, we verified that $\tilde{\gamma}$ is independent of the aggregation scale s_a . In contrast,

$$\tilde{\omega} \approx 2 \log(\mathcal{A}/(\ell_0 s_a)), \quad (4.27)$$

is a function of the aggregation scale only, independent of time and fractal dimension (Fig. 14.b). Having determined both the elongation statistics inside aggregates of size n and the spatial distribution of n , we will deduce in the following section the statistics of aggregated scalar levels c .

5. Aggregated scalar concentrations

In the preceding section, we have shown that the moments of lamella compression inside a bundle of size n follow:

$$\mu_{\rho^{-1}|n} = \frac{s_a \ell_0}{\mathcal{A}} n^{-1} \quad (5.1)$$

$$\mu_{\rho^{-2}|n} = \frac{(s_a \ell_0)^2}{\mathcal{A}^2} n^{-\tilde{\gamma}} \quad (5.2)$$

with $\tilde{\gamma} \equiv \gamma_{2,\rho^{-1}|n}$ a flow-dependent exponent varying with the fractal dimension D_1 and taking value between 1 and 2 (Fig. 14a). The variance of lamellar concentrations inside bundles thus follows:

$$\sigma_{\rho^{-1}|n}^2 = \frac{(s_a \ell_0)^2}{\mathcal{A}^2} (n^{-\tilde{\gamma}} - n^{-2}). \quad (5.3)$$

We first assume that the aggregated scalar concentration of a bundle $c|n$ can be obtained by a sum of independent and identically distributed random variables (Eq. (2.21)), whose statistics have been described previously. In doing so, we make two hypothesis. First, we assume that the elongation statistics of lamella inside a bundle of size n or among all bundles size n are comparable, which is true for large n (see Appendix C). Second, we assume that variability in bundle aggregated concentrations arises from *independent* realizations of the sum. In other words, we assume that the chaotic flow is sufficiently random to shuffle lamellar elongations between each bundles. We will show later that independence is not ensured in the deterministic Baker map.

With these hypothesis, the mean aggregated concentration is

$$\mu_{c|n} = n \cdot \frac{\sqrt{\pi} \theta_0 s_0}{s_a} \mu_{\rho^{-1}|n} = \frac{\sqrt{\pi} \theta_0 \ell_0 s_0}{\mathcal{A}}, \quad (5.4)$$

which is also the mean concentration μ_c . The variance of aggregated concentrations over bundles of similar size is

$$\sigma_{c|n}^2 \approx n \left(\frac{\sqrt{\pi} \theta_0 s_0}{s_a} \right)^2 \sigma_{\rho^{-1}|n}^2 = \frac{(\sqrt{\pi} \theta_0 \ell_0 s_0)^2}{\mathcal{A}^2} (n^{1-\tilde{\gamma}} - n^{-1}). \quad (5.5)$$

When n large, this expression further simplifies to

$$\sigma_{c|n}^2 \sim n^{1-\tilde{\gamma}}, \quad (5.6)$$

with $\tilde{\gamma} \in [1, 2]$ given by Eq. 4.26.

The scaling obtained with the independent realization hypothesis compares well with numerical simulations of aggregation in random sine flows of various heterogeneity (Fig. 16). However, it largely underestimates the scaling observed in deterministic baker map. Indeed, the simplicity and regularity of the deterministic baker map makes bundles of similar size not statistically independent. While bundle concentration still results from the addition of variable lamellar concentrations, independent realisations of the sum are not achieved due to the deterministic nature of the map, the same combinations being repeated identically in most bundles, as in the case of a unique realization. In that case, the variance of the sum is the variance of the random variable and Eq. (5.5) transforms into

$$\sigma_{c|n}^2 \sim \sigma_{\rho^{-1},n}^2 \sim n^{-\tilde{\gamma}}. \quad (5.7)$$

This scaling indeed fits more accurately the deterministic baker map simulations (Fig. 16).

To summarise, the addition of lamellar concentration levels in a bundle yields a concentration whose deviation from the mean decays algebraically with the number of lamella in the bundle

$$\sigma_{c|n}^2 \approx \frac{(\theta_0 \ell_0 s_0)^2}{\mathcal{A}^2} n^{-\xi}, \quad (5.8)$$

with $\xi = \tilde{\gamma}$ for purely deterministic flows (baker map) and $\xi = \tilde{\gamma} - 1$ for random flows (sine flow). We call ξ the *correlation* exponent, which can take values between 0 and 2 depending on the flow heterogeneity and randomness.

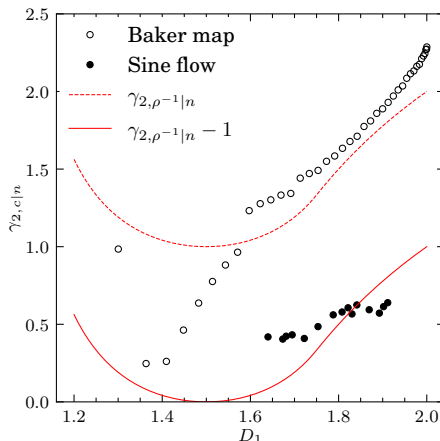


Figure 16: Scaling exponent ξ (Eq. (5.8)) of the variance of bundle concentrations knowing n estimated from simulations (dots) and theoretical predictions with the independent realisation hypothesis for the sine flow (dashed lines, $\xi = \tilde{\gamma} - 1$, Eq. (5.6)) and baker map (continuous lines, $\xi = \tilde{\gamma}$, Eq. (5.7)).

5.1. Distribution of c

We now focus on deriving the expression of the pdf of aggregated scalar concentration P_c over the flow domain. The later can be obtained from the conditional pdf of bundle aggregated concentrations knowing their size $P_{c|n}$ and the pdf of bundles size P_n by the weighted summation

$$P_c(c) = \int_n dn P_{c|n}(c) P_n(n). \quad (5.9)$$

P_n was found to be well approximated by a Gamma distribution, with moments given by the fractal characteristics of advected material lines (Eq. (4.14)). In turn, we have determined the scaling of the first two moments of bundle aggregated concentration $c|n$ (Eq. (5.8)), without specifying the precise shape of the pdf. A natural choice for $P_{c|n}$ is the log-normal distribution, since the sum of log-normally distributed random variables are known (Schwartz & Yeh 1982) to be well approximated by log-normal distributions. Adopting the log-normal shape, the parameters of the distribution are

$$\mu_{\log c|n} = \log \mu_{c|n} - \log(\sigma_{c|n}^2 / \mu_{c|n}^2 + 1) / 2 \quad (5.10)$$

$$\sigma_{\log c|n}^2 = \log(\sigma_{c|n}^2 / \mu_{c|n}^2 + 1). \quad (5.11)$$

In Fig. 17, we plot the simulated distribution of aggregated concentration levels compared to the prediction Eq. (5.9) for the baker map and sine flow. The agreement is fair in the region near μ_c , but deviates for large c . Indeed, this corresponds to lamellae with weak aggregation for which $n \approx 1$. In this region, the solitary strip pdf $P_{\rho^{-1}}$ describes well the tail of P_c because such high concentration excursions are essentially supported by isolated lamellae, while the correlated aggregation model assumes $n \gg 1$. The presence of these weakly aggregated, high concentration levels is particularly evident at high Péclet number (Fig. 17 (b)). The scalar concentration pdf is thus the combination of an aggregated core around the mean following Eq. (5.9) and tails following the isolated strip concentration pdf.

In Figs. 3c and 18, we compare the correlated aggregation model with the random aggregation model where $\mu_n \sim L(t)$ (Eq. (2.19)). The random aggregation assumption

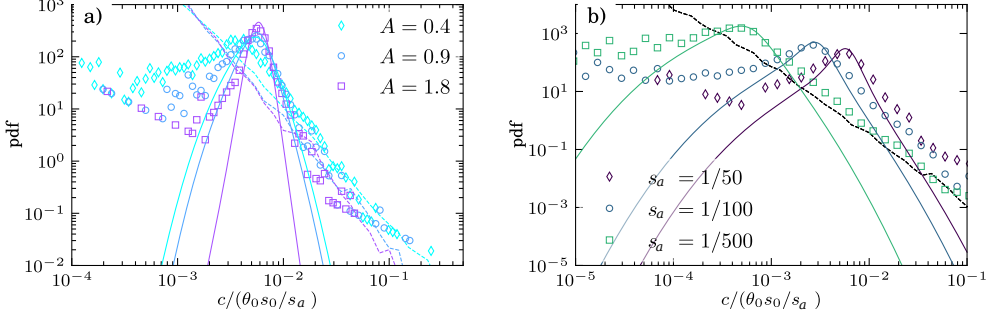


Figure 17: Distributions of aggregated scalar concentrations in the sine flow depending on a) the sine wave amplitude A ($s_a = 1/50$) and b) the aggregation scale s_a ($A = 0.9$). Dots stand for numerical simulations, continuous lines are the aggregation model (Eq. (5.9)), and the dashed lines are the isolated strip prediction (Eq. (2.6)). Simulations are all taken at the time when the total filament length reaches $L = 10^7 \ell_0$.

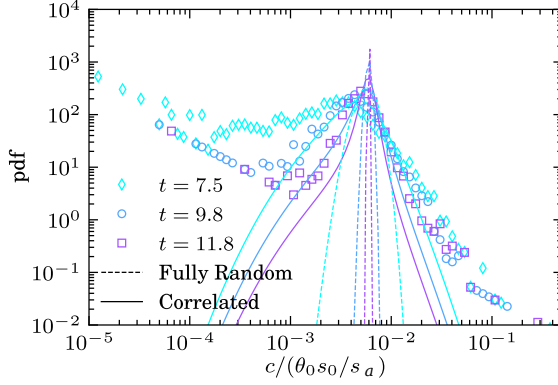


Figure 18: P_c in sine flows at several times ($A = 0.8$, $s_a = 1/50$) (dots) compared with the random aggregation (dashed lines) and correlated aggregation (continuous lines, Eq. (5.9)) models.

yields gamma pdfs that are narrowing much faster than the simulated pdfs in the sine flow. In contrast, the correlated model better captures the pdf.

From the pdf of aggregated scalar concentration, we now derive its moments. They are directly related to the pdf of n , since

$$\mu_c = \int dc \sum_n c P(c|n) P(n) = \sum_n \mu_{c|n} P(n) = \frac{\theta_0 \ell_0 s_0}{\mathcal{A}} \quad (5.12)$$

and

$$\mu_{c^2} = \int_c dc \int_n dn c^2 P(c|n) P(n) = \int_n dn \mu_{c^2|n} P(n) = \frac{(\theta_0 \ell_0 s_0)^2}{\mathcal{A}^2} (\mu_{n-\xi} + 1). \quad (5.13)$$

Thus, the scalar variance is

$$\sigma_c^2 = \frac{(\theta_0 \ell_0 s_0)^2}{\mathcal{A}^2} \mu_{n-\xi}. \quad (5.14)$$

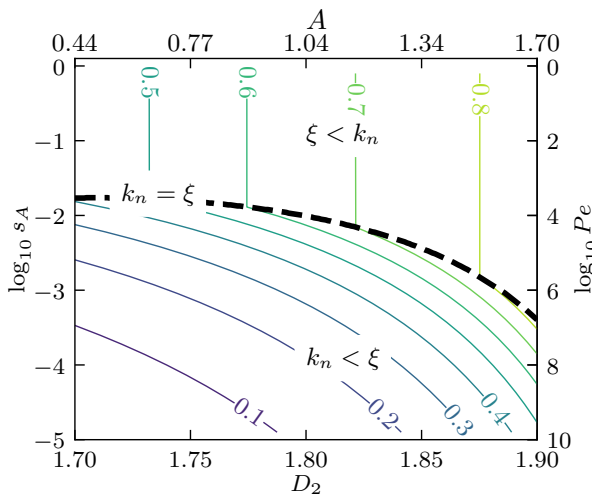


Figure 19: Evolution of the exponent $\min(k_n, \xi)$ (contours) in the sine flow for various Péclet (aggregation scale s_A) and sine amplitude A (fractal dimension D_2). k_n is obtained with Eq. (4.13) and $\xi = \tilde{\gamma} - 1$ with Eq. (4.26)

Note that, because we chose a gamma distribution for n with parameters θ_n and k_n defined in Eqs. (4.14), $\mu_{n^{-\xi}}$ is not defined for all D_2 . Indeed, the gamma distribution admits a power law tail at small n with exponent $k_n - 1$, which affects the value of negative moments: when $k_n(D_2) < \xi(D_2)$, $\mu_n^{-\xi}$ does not exist. However, because fully chaotic flows are space-filling ($D_0 = 2$), we must have $n \geq 1$ at late time. Thus, we restrict the pdf of n to $n \geq 1$ and get

$$\mu_{n^{-\xi}} \sim (\theta_n)^{-\min(k_n, \xi)} \quad (5.15)$$

An intuitive understanding of this equation can be formulated as follows. If the spatial heterogeneity of n is moderate ($\xi < k_n$), the average of $n^{-\xi}$ is affected by all values of n in the distribution. In contrast, if the heterogeneity is stronger ($\xi > k_n$), the probability of having low aggregation regions ($n \approx 1$) is high and controls the value of $\mu_{n^{-\xi}}$. In that case, the average does not scale anymore with ξ , but rather with the parameter k_n , explaining the minimum in the exponent. The value of the exponent depending on Péclet number and fractal dimension is plotted in Figure 19 for the sine flow. In such random flow, the exponent takes values between 0 and 1. For high Péclet numbers and low fractal dimension, $\mu_{n^{-\xi}}$ is governed by weakly aggregated regions and $\min(k_n, \xi) = k_n$. In contrast, for low Péclet number and large fractal dimension, the whole distribution of n plays a role in the determination of $\mu_{n^{-\xi}}$ and $\min(k_n, \xi) = \xi$.

Combining Eq. (5.15) and Eq. (4.14) provides the asymptotic scalar variance decay as a function of the domain area \mathcal{A} , the elongation of material lines $L(t)$, and the aggregation scale $s_a = \sqrt{2\pi} s_B$:

$$\sigma_c^2(t) = \left(\frac{L(t) s_a (\sqrt{\mathcal{A}} s_a^{D_2-2} - 1)}{\mathcal{A}} \right)^{-\min(k_n, \xi)} \sim L(t)^{-\min(k_n, \xi)}. \quad (5.16)$$

Thus, in a correlated aggregation scenario, the decay exponent of scalar variance is found to be a fraction of the growth exponent of material lines; respectively $\log 2$ and $\mu_\lambda + \sigma_\lambda^2/2$ in the baker map and sine flow.

Eq. (5.16) suggests that the existence of correlations in the aggregation process may be

envisioned as a retardation of the purely random aggregation scenario (Eq. (2.22)). From this perspective, the effective number of *random* aggregation events $L(t)^{\min(k_n, \xi)}$ is smaller than the total number of aggregation $L(t)$, because the correlation exponent $\min(k_n, \xi)$ is generally smaller than one (see Fig. 19).

In contrast, the random aggregation model (Eq. 2.22) clearly overestimates the variance decay rate in the sine flow. This is explained by the correlated nature of aggregation which is less efficient at homogenising concentration levels than a completely random addition. In other words, small concentration levels have a higher probability of coalescing with other small concentrations than with high concentrations, retarding the homogenisation of the mixture. Indeed, the correlated aggregation model proposed herein (Eq. (5.16)) shows decay rates closer to the numerical observations. Solitary lamella model still outperforms the correlated aggregation framework in predicting scalar decay rate, because the latter is dominated by weakly aggregated regions of the flow. These regions are poorly described by statistics obtained in the large- n limit (e.g. Eq. (5.5)).

A different picture is observed for scalar decay rates obtained in the baker map (Fig. 20b), because of the deterministic nature of the map. The solitary lamella model is accurate for fractal dimensions $D_1 < 1.6$, where stretching heterogeneity is important and weakly aggregated regions of the flow dominate scalar fluctuations. For $D_1 > 1.6$, the isolated lamella model underpredicts scalar decay due to aggregation effects as explained in the following. The random aggregation scenario predicts an invariant scalar decay rate ($\gamma_{2,c} = \log 2$) equal to the growth rate of material lines. It thus overpredicts the observed decay rates for $D_1 < 1.8$ and underpredicts it at larger values of D_1 . Interestingly, when the flow tends to the uniform case $a \rightarrow 0.5$ ($D_1 \rightarrow 2$), simulations yields scalar decay rates of $2 \log 2$, larger than the decay rate of isolated lamella. This acceleration of mixing by aggregation is a pure consequence of the determinism nature of the map, and is well captured by the correlated aggregation scenario (Eq. (5.7)). However, for all baker maps with $D_1 < 1.9$ ($a < 0.2$), $k_n < \xi$ and scalar fluctuations are mainly governed by the regions where $n \sim 1$ for which the correlated aggregation theory is not expected to be accurate. This explains the limited range of validity of the correlated aggregation theory for describing scalar decay rates in the deterministic baker map.

Finally, note that the simulations do not show the super-exponential decay of scalar fluctuations classically observed for the uniform stretching rate at $a = 0.5$. In fact, the reconstruction of the scalar field by a summation of lamellar maximum concentrations on a fixed grid (Eq. (3.4)) impedes the apparition of the super-exponential mode. As $a \rightarrow 0.5$, all lamella are subjected to similar stretching rates around $\log 2$, thus yielding a scalar variance decaying as $2 \log 2$.

6. Conclusions

Scalar mixing by incompressible smooth two-dimensional chaotic flows leads to the emergence of two coupled phenomena which are the elongation of interfaces by stretching, and their aggregation and coalescence at the Batchelor scale by compression. In turbulent scalar mixing, aggregation was well captured by random addition rules (Duplat & Villermaux 2008). Here, we show that for smooth chaotic flows in the Batchelor range, aggregation is highly correlated. This correlated aggregation process significantly reduces the flow mixing efficiency compared to a random hypothesis, maintaining it close to the mixing efficiency obtained for solitary lamellae and explaining the observed monotonic exponential decay of scalar variance before and after coalescence time (Fereday *et al.* 2002).

Using two-dimensional chaotic flows as a reference, we measured the aggregation rate of exponentially stretched material lines across a broad range of chaotic flow regimes. We

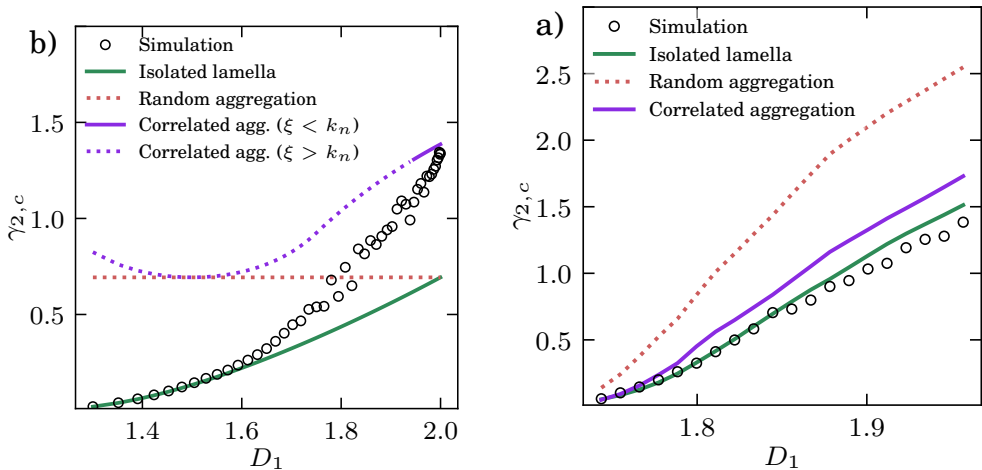


Figure 20: Decay exponent γ_2 of the variance of aggregated scalar levels with time, as a function of fractal dimension D_1 for the a) random sine flow and b) baker map. Dots stand for numerical simulations and lines from theoretical predictions for isolated lamellae (Eq. (2.17) and exponents of $\mu_{\rho^{-1}}$ in Tables 1 and 2), random aggregation (Eq. (2.22) and exponents of $1/\mu_{\rho}$ in Tables 1 and 2) and correlated aggregation (Eq. (5.14)).

showed that the most elongated lamellae are also the most aggregated ones, due to the fact that larger compression rates attract larger flow regions. The link between elongation and compression, induced by incompressibility, hence generates a direct correlation between elongation and aggregation. The heterogeneity in stretching rates therefore controls the heterogeneity of the number of lamellae in bundles.

We showed that the statistics of aggregated lamella numbers can be exactly predicted from the fractal dimensions of the elongated material line. We then derived a general theoretical framework that captures the effect of correlated aggregation, where lamellae of similar stretching aggregate preferentially, and predict the pdfs of aggregated scalar levels. We find that correlated aggregation can be uniquely characterised by single correlation exponent $\xi \in [0, 1]$, which provides a measure of the *effective* number of aggregation events, compared to the *total* number. In that sense, correlated aggregation delays the route to uniformity compared to a fully random hypothesis, although it does not alter the fundamental nature of the aggregation process (Villermaux & Duplat 2003).

Our results apply for two-dimensional fully chaotic flows in the Batchelor regime, that is, for smooth velocity fields below the integral scale. These flow fields are representative of a large class of flows, including notably porous media flows (Heyman *et al.* 2020; Souzy *et al.* 2020), geophysical flows, and turbulent flows at high Schmidt number. We have also considered small periodic flow domains where no large scale scalar gradients can appear. When scalar length scales can develop beyond the integral velocity scale in smooth flows, mixing is controlled *globally* by the slowest dispersing modes (Haynes & Vanneste 2005; Tsang *et al.* 2005). The aggregation rules determined herein are not supposed to change above the velocity scale. Thus, it is in principle possible to obtain the statistics of larger scale scalar fields by the summation of individual lamella. To do so, one may consider the mean density of aggregation $\mu_n(t)$ (Eq. (4.4)) to vary spatially through macrodispersion, while microscale fluctuations would remain governed by Eq. (4.11). Note that similar ideas

were used to predict the evolution of a dispersing scalar plume in a two-dimensional porous media (Le Borgne *et al.* 2015).

It should also be possible to extend the correlated aggregation theory to three-dimensional flows that produce two-dimensional sheets (Martínez-Ruiz *et al.* 2018; Ngan & Vanneste 2011; Meunier & Villiermaux 2022), that aggregate at late time due to folding. These flows have a unique negative Lyapunov exponent, the mean compression rate normal to the sheets, and thus also simplify to the one-dimensional Lagrangian stretching framework on which aggregation models are framed.

REFERENCES

- AREF, HASSAN 1984 Stirring by chaotic advection. *Journal of Fluid Mechanics* **143**, 1–21.
- BALKOVSKY, E & FOUXON, A 1999 Universal long-time properties of lagrangian statistics in the batchelor regime and their application to the passive scalar problem. *Physical Review E* **60** (4), 4164.
- BATCHELOR, G. K. 1959 Small-scale variation of convected quantities like temperature in turbulent fluid part I. general discussion and the case of small conductivity. *J. Fluid Mech.* **5** (1), 113–133.
- DUPLAT, J., JOUARY, A. & VILLERMAUX, E. 2010 Entanglement rules for random mixtures. *Phys. Rev. Lett.* **105**, 034504.
- DUPLAT, J. & VILLERMAUX, E. 2008 Mixing by random stirring in confined mixtures. *J. Fluid Mech.* **617**, 51–86.
- FALKOVICH, G, GAWĘDZKI, K.ĘDZKI, K & VERGASSOLA, MASSIMO 2001 Particles and fields in fluid turbulence. *Reviews of modern Physics* **73** (4), 913.
- FARMER, J DOYNE, OTT, EDWARD & YORKE, JAMES A 1983 The dimension of chaotic attractors. *Physica D: Nonlinear Phenomena* **7** (1-3), 153–180.
- FEREDAY, DR, HAYNES, PH, WONHAS, A & VASSILICOS, JC 2002 Scalar variance decay in chaotic advection and batchelor-regime turbulence. *Physical Review E* **65** (3), 035301.
- FINN, JOHN M & OTT, EDWARD 1988 Chaotic flows and fast magnetic dynamos. *The Physics of fluids* **31** (10), 2992–3011.
- GARRETT, CHRISTOPHER 1983 On the initial streakiness of a dispersing tracer in two-and three-dimensional turbulence. *Dynamics of Atmospheres and Oceans* **7** (4), 265–277.
- GIONA, M, CERBELLI, S & ADROVER, A 2001 Geometry of reaction interfaces in chaotic flows. *Physical review letters* **88** (2), 024501.
- GRASSBERGER, PETER 1983 Generalized dimensions of strange attractors. *Physics Letters A* **97** (6), 227–230.
- HAYNES, PETER H & VANNESTE, JACQUES 2005 What controls the decay of passive scalars in smooth flows? *Physics of Fluids* **17** (9), 097103.
- HEYMAN, J., LESTER, D. R. & LE BORGNE, T. 2021 Scalar signatures of chaotic mixing in porous media. *Phys. Rev. Lett.* **126**, 034505.
- HEYMAN, JORIS, LESTER, DANIEL R., TURUBAN, RÉGIS, MÉHEUST, YVES & LE BORGNE, TANGUY 2020 Stretching and folding sustain microscale chemical gradients in porous media. *Proceedings of the National Academy of Sciences* **117** (24), 13359–13365.
- LE BORGNE, T., DENTZ, M. & VILLERMAUX, E. 2015 The lamellar description of mixing in porous media. *J. Fluid Mech.* **770**, 458–498.
- LE BORGNE, T., HUCK, P. D., DENTZ, M. & VILLERMAUX, E. 2017 Scalar gradients in stirred mixtures and the deconstruction of random fields. *J. Fluid Mech.* **812**, 578–610.
- LESTER, D. R., DENTZ, M. & LE BORGNE, T. 2016 Chaotic mixing in three-dimensional porous media. *J. Fluid Mech.* **803**, 144–174.
- LESTER, D. R., METCALFE, G. & TREFRY, M. G. 2013 Is chaotic advection inherent to porous media flow? *Phys. Rev. Lett.* **111**, 174101.
- MARTÍNEZ-RUIZ, DANIEL, MEUNIER, PATRICE, FAVIER, BENJAMIN, DUCHEMIN, LAURENT & VILLERMAUX, EMMANUEL 2018 The diffusive sheet method for scalar mixing. *Journal of Fluid Mechanics* **837**, 230–257.
- MEUNIER, P. & VILLERMAUX, E. 2010 The diffusive strip method for scalar mixing in two dimensions. *J. Fluid Mech.* **662**, 134–172.
- MEUNIER, PATRICE & VILLERMAUX, EMMANUEL 2022 The diffuselet concept for scalar mixing. *Journal of Fluid Mechanics* **951**, A33.

- NGAN, KEITH & VANNESTE, JACQUES 2011 Scalar decay in a three-dimensional chaotic flow. *Physical Review E* **83** (5), 056306.
- OTT, EDWARD & ANTONSEN JR, THOMAS M 1989 Fractal measures of passively convected vector fields and scalar gradients in chaotic fluid flows. *Physical Review A* **39** (7), 3660.
- OTTINO, J.M. 1990 Mixing, chaotic advection, and turbulence. *Annu. Rev. Fluid Mech.* **22**, 207–253.
- PIERREHUMBERT, RAYMOND T 1994 Tracer microstructure in the large-eddy dominated regime. *Chaos, Solitons & Fractals* **4** (6), 1091–1110.
- RANZ, WILLIAM E. 1979 Applications of a stretch model to mixing, diffusion, and reaction in laminar and turbulent flows. *AIChE J.* **25** (1), 41–47.
- REDNER, SIDNEY 1990 Random multiplicative processes: An elementary tutorial. *Am. J. Phys* **58** (3), 267–273.
- ROTHSTEIN, D, HENRY, E & GOLLUB, JERRY P 1999 Persistent patterns in transient chaotic fluid mixing. *Nature* **401** (6755), 770–772.
- SCHWARTZ, STUART C & YEH, YU-SHUAN 1982 On the distribution function and moments of power sums with log-normal components. *Bell System Technical Journal* **61** (7), 1441–1462.
- SINAI, YA G & YAKHOT, VICTOR 1989 Limiting probability distributions of a passive scalar in a random velocity field. *Physical review letters* **63** (18), 1962.
- SOUZY, M., LHUISSIER, H., MÉHEUST, Y., LE BORGNE, T. & METZGER, B. 2020 Velocity distributions, dispersion and stretching in three-dimensional porous media. *Journal of Fluid Mechanics* **891**, A16.
- SUKHATME, JAI 2004 Probability density functions of decaying passive scalars in periodic domains: An application of sinai-yakhot theory. *Physical Review E* **69** (5), 056302.
- SUKHATME, JAI & PIERREHUMBERT, RAYMOND T 2002 Decay of passive scalars under the action of single scale smooth velocity fields in bounded two-dimensional domains: From non-self-similar probability distribution functions to self-similar eigenmodes. *Physical Review E* **66** (5), 056302.
- TANG, XIAN ZHU & BOOZER, ALLEN H 1996 Finite time lyapunov exponent and advection-diffusion equation. *Physica D: Nonlinear Phenomena* **95** (3-4), 283–305.
- THIFFEAULT, JEAN-LUC 2004 Stretching and curvature of material lines in chaotic flows. *Physica D: Nonlinear Phenomena* **198** (3), 169 – 181.
- TSANG, YUE-KIN, ANTONSEN JR, THOMAS M & OTT, EDWARD 2005 Exponential decay of chaotically advected passive scalars in the zero diffusivity limit. *Physical Review E* **71** (6), 066301.
- VILLERMAUX, EMMANUEL 2012 On dissipation in stirred mixtures. *Advances in applied mechanics* **45**, 91–107.
- VILLERMAUX, EMMANUEL 2019 Mixing versus stirring. *Annu. Rev. Fluid Mech.* **51** (1), 245–273.
- VILLERMAUX, EMMANUEL & DUPLAT, JÉRÔME 2003 Mixing as an aggregation process. *Physical review letters* **91** (18), 184501.
- WARHAFT, ZELLMAN 2000 Passive scalars in turbulent flows. *Annu. Rev. Fluid Mech.* **32** (1), 203–240.
- WONHAS, A & VASSILICOS, JC 2002 Mixing in fully chaotic flows. *Physical Review E* **66** (5), 051205.

Acknowledgements. JH, TLB and PD acknowledge the Europe Research Council under the grant 101042466 (CHORUS). TLB and EV acknowledge the H2020 MSCA ITN program, under the grant 956457 (COPERMIX). Three anonymous reviewers are thanked for contributions to the manuscript.

Funding. Funded by the European Union (ERC, CHORUS, 101042466)

Declaration of interests. The authors report no conflict of interest.

Data availability statement. The data and codes to reproduce the findings of this study are openly available in Github at <https://github.com/jorishey1234/aggregation> or upon reasonable request to joris.heyman@univ-rennes.fr

Author ORCIDs. J. Heyman, <https://orcid.org/0000-0002-0327-7924>; T. Le Borgne, <https://orcid.org/0000-0001-9266-9139>; E. Villermaux, <https://orcid.org/0000-0001-5130-4862>; P. Davy, <https://orcid.org/0000-0002-6648-0145>

Appendix A. Stretching statistics and averaging

In random chaotic flows, varying stretching rates are experienced by fluid elements (Lester *et al.* 2013). Because of the multiplicative nature of stretching, the log-elongation of material

elements $\log \rho$ is well approximated in ergodic chaotic flows by a sum of iid random variables, that converges towards the normal distribution with mean $\mu_\lambda t$ and variance $\sigma_\lambda^2 t$ (Meunier & Villiermaux 2022).

Thus, the elongation ρ of material elements may be expected to follow the log-normal distribution

$$P_{\rho,0}(\rho) \approx \frac{1}{\rho \sqrt{2\pi\sigma_\lambda^2 t}} \exp\left(-\frac{(\log \rho - \mu_\lambda t)^2}{2\sigma_\lambda^2 t}\right). \quad (\text{A } 1)$$

Non-asymptotic stretching statistics can differ substantially from this limiting behavior. For instance, the baker map has a binomial distribution of elongations

$$P_{\rho,0}(\rho = (1-a)^k a^{t-k}) = \binom{t}{k} (1-a)^k a^{t-k}, \text{ for } k = 0 \dots t, \quad (\text{A } 2)$$

which tends to a lognormal distribution with $\mu/t = -a \log(a) - (1-a) \log(1-a)$ and $\sigma_\lambda^2/t = a(1-a)(\log(1-a) - \log(a))^2$.

Note also that, because of the multiplicative nature of elongation (Redner 1990), the pdf of ρ (and ρ^{-1}) is highly sensitive to the tails of $P_{\log \rho}$, which may converge only slowly to the Gaussian prediction depending on the flow heterogeneity. However, for the range of sine flow amplitudes used in this study ($A \in [0.4, 1.8]$), such limitations are relatively weak.

Statistics of lamellar concentrations in the material line can then be obtained by suitable ensemble averaging (denoted by angle brackets) over this distribution. Depending on how sampling is performed through the material line, different moments are obtained. Uniform sampling on the *initial* filament prior elongation leads to the distribution $P_\rho(\rho)$ (Eq. (A 1)) with main moments summarized in Table 1. In contrast, uniform sampling on a the *final* elongated material line of length L , denoted by $\mu_{\bullet,L}$ leads to the weighted pdf $P_{\rho,L} \sim \rho P_\rho$. $P_{\rho,L}$ is thus also lognormal, but with different mean, $(\mu_\lambda + \sigma_\lambda^2)t$. Uniform sampling on the final material line gives a stronger weights to highly elongated part of the material line than uniform sampling on the initial filaments. Moments of $\log \rho$, ρ and ρ^{-1} are summarized in Tables 1 for sine flow and 2 for the baker map for initial and final sampling. Note that we impose $\rho \geq 1$ since the one-dimensional lamellar framework is valid only when lamellae elongates in the y direction. This lower bound creates a particular scaling of moments of ρ^{-1} when σ_λ^2 is larger than μ , that is when weak stretching rates dominate the ensemble average.

Appendix B. Fractal dimensions in the baker map

The fractal dimension of order q of the measure p is obtained with (Grassberger 1983):

$$D_q - 1 = \lim_{\epsilon \rightarrow 0} \frac{1}{q-1} \frac{\log I_q(\epsilon)}{\log \epsilon}, \quad I_q(\epsilon) \equiv \sum_k^{N=\mathcal{L}/\epsilon} p_k^q, \quad (\text{B } 1)$$

where the subtraction of 1 on the left hand side accounts for the counting of one-dimensional structures (lamellae) in a two-dimensional domain. This definition implies the following spatial scaling of the integral of the measure:

$$I_q(\epsilon) \sim \epsilon^{(q-1)(D_q-1)}. \quad (\text{B } 2)$$

In the baker map, the integral of the measure can then be computed by summing its value on the two replicates created by the map,

$$I_q(\epsilon) = I_{q,a}(\epsilon) + I_{q,1-a}(\epsilon). \quad (\text{B } 3)$$

	$\log \rho$	ρ	ρ^{-1}
μ_{\bullet}	$\mu\lambda t$	$e^{(\mu\lambda + \sigma_\lambda^2/2)t}$	$\begin{cases} e^{-(\mu - \sigma_\lambda^2/2)t} & \text{if } \mu\lambda \geq \sigma_\lambda^2 \\ e^{-\mu^2/(2\sigma_\lambda^2)t} & \text{if } \mu\lambda \leq \sigma_\lambda^2 \end{cases}$
μ_{\bullet^2}	$\sigma_\lambda^2 t$	$e^{(2\mu\lambda + 2\sigma_\lambda^2)t}$	$\begin{cases} e^{-2(\mu - \sigma_\lambda^2)t} & \text{if } \mu\lambda \geq 2\sigma_\lambda^2 \\ e^{-\mu^2/(2\sigma_\lambda^2)t} & \text{if } \mu\lambda \leq 2\sigma_\lambda^2 \end{cases}$
$\mu_{\bullet,L}$	$(\mu + \sigma_\lambda^2)t$	$e^{(\mu\lambda + 3\sigma_\lambda^2/2)t}$	$e^{(-\mu\lambda - \sigma_\lambda^2/2)t}$
$\mu_{\bullet^2,L}$	$\sigma_\lambda^2 t$	$e^{(2\mu\lambda + 4\sigma_\lambda^2)t}$	$\begin{cases} e^{-2\mu\lambda t} & \text{if } \mu\lambda \geq \sigma_\lambda^2 \\ e^{-(\mu + \sigma_\lambda^2)^2/(2\sigma_\lambda^2)t} & \text{if } \mu\lambda \leq \sigma_\lambda^2 \end{cases}$

Table 1: Moments of log-normally distributed stretching sampled over infinitesimal fluid elements ($\langle \bullet \rangle_0$), material line ($\langle \bullet \rangle_L$).

	$\log \rho$	ρ	ρ^{-1}
μ_{\bullet}	$(-a \log(a) - (1-a) \log(1-a))t$	2^t	$(1-2a+2a^2)^t$
μ_{\bullet^2}	$a(1-a)(\log(1-a) - \log(a))^2 t$	$-$	$(1-3a+3a^2)^t$

Table 2: Moments of binomial distributed stretching sampled over infinitesimal fluid elements ($\langle \bullet \rangle_0$), material line ($\langle \bullet \rangle_L$).

We observe that

$$I_{q,a}(a\epsilon) = I_{q,1-a}((1-a)\epsilon) = \sum_k^{N=1/\epsilon} \left(\frac{pk}{2}\right)^q, \quad (\text{B } 4)$$

where the factor 1/2 comes from the normalisation of the measure due to the doubling of n . Thus

$$I_{q,a}(\epsilon) = I_q(\epsilon/a)2^{-q} \text{ and } I_{q,1-a}(\epsilon) = I_q(\epsilon/(1-a))2^{-q}. \quad (\text{B } 5)$$

Replacing the last expression in (B 3) yields

$$I_q(\epsilon) = 2^{-q} \epsilon^{(q-1)D_q} \left(a^{-(q-1)(D_q-1)} + (1-a)^{-(q-1)(D_q-1)} \right) \quad (\text{B } 6)$$

Using the scaling $I_q(\epsilon) \sim \epsilon^{(q-1)D_q}$, thus provide a transcendental equation for D_q independently of ϵ :

$$2^q = \left(a^{-(q-1)(D_q-1)} + (1-a)^{-(q-1)(D_q-1)} \right), \quad (\text{B } 7)$$

the solution of which is explicit for $q = 0$ and $q = 1$:

$$D_0 = 2, \quad D_1 = 1 + \frac{2 \log 2}{\log(a^{-1} + (1-a)^{-1})}. \quad (\text{B } 8)$$

Note that the solution for $q = 1$ is obtained with Bernouilli's rule by differentiating (B 7) with respect to q , and taking the limit $q \rightarrow 1$.

Appendix C. Single and multiple bundles statistics.

The variability of a set of random numbers is always greater than the average variability of a subset of these numbers. Thus, the stretching variance *among* bundles of similar sizes—denoted $\sigma_{\rho^{-1},n}^2$ —is always larger than the average stretching variance inside the bundle (Eq. (5.3)). We have

$$\sigma_{\rho^{-1},n}^2 = \left(\frac{n}{n-1} \right) \sigma_{\rho^{-1}|n}^2. \quad (\text{C } 1)$$

For instance, for bundles made of two lamellae, we expect $\sigma_{\rho^{-1},n}^2$ to be twice larger as $\sigma_{\rho^{-1}|n}^2$ given by Eq. (5.3). The difference between the statistics of the set and its subset tends to reduce at large n , where $\sigma_{\rho^{-1}|n}^2 \rightarrow \sigma_{\rho^{-1},n}^2$. For $n = 1$, both $\sigma_{\rho^{-1}|n}^2$ and $n - 1$ cancel out, so that the previous equation is undetermined.

Assuming that bundles of similar size have independent stretching histories, the variability of the aggregated scalar concentration is obtained from independent realisations of the random sum (Eq. (3.4)). Thus, the variance of $c|n$ reads

$$\sigma_{c|n}^2 = n \left(\frac{\sqrt{\pi}\theta_0 s_0}{s_a} \right)^2 \sigma_{\rho^{-1},n}^2 = \left(\frac{\sqrt{\pi}\theta_0 s_0}{s_a} \right)^2 \sigma_{\rho^{-1}|n}^2 \left(\frac{n^2}{n-1} \right) = \frac{(\sqrt{\pi}\theta_0 \ell_0 s_0)^2}{\mathcal{A}^2} \left(\frac{n^{2-\tilde{\gamma}} - 1}{n-1} \right). \quad (\text{C } 2)$$

When n is large, however, we recover

$$\sigma_{c|n}^2 \sim n^{-\tilde{\gamma}+1}, \quad (\text{C } 3)$$